Topology optimisation of architected cellular materials from additive manufacturing: Analysis, design, and experiments

Marco Montemurro *, Giulia Bertolino, Enrico Panettieri

Arts et Métiers Institute of Technology, Université de Bordeaux, CNRS, INRA, Bordeaux INP, HESAM Université, I2M UMR 5295, F-33405 Talence, France

Keywords:
Topology optimisation
NURBS hyper-surfaces
Lattice structures
Architected cellular materials
Additive manufacturing
Three-point bending test

A B S T R A C T

This work deals with an experimental/numerical validation of the optimised topologies found through a special density-based topology optimisation (TO) method wherein the topological descriptor, i.e., the pseudo-density field, is represented through a non-uniform rational basis spline (NURBS) hyper-surface. The framework is that of multi-scale TO methods to design architected cellular materials (ACMs). Specifically, in the most general case, the topological variables are defined at the scale of the representative volume element (RVE) of the ACM and at the macroscopic scale of the structure. The transition among scales is performed via a numerical homogenisation scheme based on the strain energy of elements. The proposed formulation exploits the properties of NURBS entities to determine the relationships occurring among the topological variables defined at different scales to correctly state the optimisation problem and to satisfy the hypotheses at the basis of the homogenisation method. Three design cases are considered: in the first one, TO is performed only at the macroscopic scale; in the second one, TO is performed only at the RVE scale; in the last one, TO is performed simultaneously at both scales. Multiple design requirements related to lightness, scale separation condition (to ensure the validity of the results of the homogenisation method) and minimum printable size are included in the problem formulation. Particularly, the last two requirements are implicitly satisfied by controlling the integer parameters of the NURBS entity (describing the pseudo-density field at each scale) without introducing explicit optimisation constraints. The multi-scale TO strategy is applied to a structure made of ACM subject to three-point bending test-like boundary conditions: for each design case, the optimised topology is manufactured through stereo-lithography and a comparison between experimental and numerical results (obtained through non-linear analysis conducted a posteriori on the optimised topology) is performed to assess the effectiveness of the approach.

1. Introduction

In the last two decades, architected cellular materials (ACMs) have attracted the interest of the scientific community and are increasingly employed in different sectors, like aerospace, automotive, biomechanical, energetic, etc., due to the possibility of conceiving the micro/meso structure to get suited performances, e.g., in terms of high specific stiffness, specific strength, high permeability, excellent energy absorption and damping capabilities and thermal insulation.

To this end, the scientific community is developing different approaches to optimise ACMs: parametric optimisation of the geometrical variables of pre-defined representative volume element (RVE) topologies [1,2], topology optimisation (TO) of the RVE to satisfy a given macroscopic elastic behaviour [3–7] and TO of the ACM at multiple scales [8–18]. TO is, undoubtedly, the most promising approach [19–21] to perform the concurrent topology and material optimisation because it allows optimising both the distribution of the material and the properties of the material at the macroscopic scale, these latter depending on the topology of the RVE at the lower scale (microscopic or mesoscopic, depending on the problem at hand). Moreover, when the problem is stated in the most general way, the optimisation of the topology of the ACM at multiple scales allows avoiding the introduction of pre-defined geometries of the RVE: in this way, a wider design space can be explored and general, efficient solutions can be found. The basic idea behind the multi-scale TO of an ACM is that the material is iteratively removed from the design domain (at each scale) and redistributed in order to minimise a prescribed cost function by satisfying the set of design requirements. Different TO methods have been proposed in the literature to carry out the multi-scale TO of ACMs, like, for instance, the level-set method [22,23], the density-based TO method making use of the solid isotropic material

* Corresponding author.
E-mail addresses: marco.montemurro@ensam.eu, marco.montemurro@u-bordeaux.fr (M. Montemurro).

https://doi.org/10.1016/j.istruc.2022.12.032

Acronyms

3PBT	Three-point bending test
ACM	Architected cellular material
BC	Boundary condition
CAD	Computer aided design
CNLPP	Constrained non-linear programming problem
CP	Control point
DC	Design case
DC1	First design case
DC2	Second design case
DC3	Third design case
DOF	Degree of freedom
FE	Finite element
GCMMA	Globally-convergent method of moving asymptotes
NURBS	Non-uniform rational basis spline
RVE	Representative volume element
SANTO	SIMP and NURBS for topology optimisation
SEHM	Strain energy-based homogenisation method
SIMP	Solid isotropic material with penalisation
SLA	Stereo-lithography
STL	Standard tessellation language
TO	Topology optimisation

with penalisation (SIMP) approach [3,24] (and its improved version wherein uncertainty on material properties and boundary conditions is integrated in the problem formulation [25–28]) or the bidirectional evolutionary structural optimisation method [29]. The above strategies can be applied, simultaneously, at the upper scale (i.e., that of the structure) and at lower scale (i.e., that of the RVE), or just at this latter, with the aim of determining the optimal configuration of the RVE showing a prescribed macroscopic behaviour, e.g., prescribed stiffness with the least mass as proposed in [30], maximum shear stiffness with a prescribed volume [31], or unconventional properties, like negative Poisson's ratio with a prescribed volume [4]. For more details on the multi-scale TO of ACMs, the interested reader is addressed to the review article by Wu et al. [32].

Regardless of the adopted approach, the assessment of the effectiveness of multi-scale TO algorithms can be done either numerically on meaningful benchmarks problems or experimentally by means of dedicated tests. In the following of this introduction, a brief survey about the experimental validation of optimised solutions obtained through TO methods available in the literature is presented. In particular, the discussion is limited to the well-known three-point bending test (3PBT), which is used to assess the effectiveness of some 2D and 3D benchmark problems subject to the same boundary conditions (BCs) of the 3PBT.

Mohan and Simhambhatla [33] proposed a numerical framework for TO and the corresponding experiments. The optimisation is carried out through a density-based TO algorithm making use of the SIMP penalisation scheme. The problem of minimising the compliance of a structure (submitted to 3PBT-like BCs) is considered with a constraint on the volume fraction of the solid phase. The topological variables are defined only at the macroscopic scale and a manufacturability constraint is applied *a posteriori* to the optimised topology to eliminate the elements belonging to those topological branches whose thickness is smaller than the one prescribed by the minimum printable size.

Rashid et al. [34] employed the bidirectional evolutionary structural optimisation method to optimise the topology of the RVE of a simple beam subject to 3PBT-like BCs. The optimisation problem was formulated in terms of compliance minimisation subject to a constraint on the volume, and experimental tests were performed on two beams for which two different RVE topologies were used. The optimised specimens were fabricated through selective laser melting. The experimental tests were conducted to compare the mechanical response of solid specimens with the one of samples composed of the optimised RVE, in terms of load vs. displacements curves. Moreover, the obtained configurations were also investigated in terms of energy absorption capability.

Zhang and Yanagimoto [35] dealt with the problem of optimising sandwich-like structures, wherein the core is composed of repetitive dome units filled with micro-lattice. The goal of the optimisation process was to find the optimal distribution of the micro-lattice at the macroscopic scale that minimises the total compliance subject to a constraint on the volume. The asymptotic homogenisation technique was exploited to calculate the equivalent elastic properties of the ACM at the upper scale. Numerical and experimental results were compared for different types of structures. The experimental data showed that the maximal energy absorption under 3PBT-like BCs is achieved by the graded dome micro-lattice structures with high density.

Zhang et al. [36] proposed a methodology to get optimised structures (subject to 3PBT-like BCs) made of graded ACMs. Particularly, the RVE of the ACMs had a predefined topology (selected from a given database). A preliminary campaign of homogenisation analyses was carried out to determine the law to be used at the macroscopic scale to penalise the stiffness tensor of the equivalent homogeneous material (replacing the ACM at this scale) as a function of the relative density of the RVE. In this way, at the end of the optimisation process one can obtain a graded (possibly optimised) ACM. Experimental tests were conducted on specimens made of polylactic acid by considering different topologies of the RVE.

A similar study on graded ACMs was proposed by Kim and Park [37] who made use of the density-based TO method based on the SIMP approach to perform multi-scale TO. The optimised samples were fabricated by digital light processing and then submitted to 3PBT-like BCs.

By taking inspiration from the main idea presented in the above works, this study aims to provide an experimental validation of the computer aided design (CAD)-compatible density-based TO method reformulated in the framework of non-uniform rational basis spline (NURBS) hyper-surfaces [38–40]. Particularly, the general theoretical/numerical framework to optimise the topology of ACMs at multiple scales, recently presented in [6,18], is here applied to a structure subject to 3PBT-like BCs. The multi-scale TO method presented in [6,18] is based on: (a) the NURBS entities to represent the topological descriptor at both the RVE (lower) scale and the macroscopic (upper) scale; (b) the strain energy-based homogenisation method (SEHM) to set the link between the scales of the problem (only weak coupling among scales is considered).

Unlike the approaches used in [33–37], the problem formulation presented in this work is general and include different design requirements and different design cases (DCs) corresponding to just as many original features.

Firstly, three DCs are considered, depending on the scales involved in the problem formulation at which the topological descriptor, i.e., the pseudo-density field, is defined. In the first DC, the topological descriptor is defined only at the upper scale of the continuum. In the second DC, the topological descriptor is introduced only at the lower scale of the continuum. In the last DC, the topological descriptor is introduced at both lower and upper scales.

Secondly, depending on the DC at hand, different requirements are involved in the problem formulation. For instance, in the most general case, wherein the topological descriptor is defined at all the problem scales, the design requirements include: a constraint on the overall mass of the structure, a constraint on the volume fraction of the solid phase of the RVE of the ACM, a constraint on the minimum member size (which is related to the minimum printable size that can be manufactured through the additive manufacturing process), a constraint on the scale

separation condition [18] (to ensure the validity of the results of the SEHM).

Lastly, for each DC, the optimised solution is fabricated through stereo-lithography (SLA) process and tested via 3PBT according to ASTM norm [41]. Moreover, by exploiting the properties of NURBS hyper-surfaces, the boundary of the optimised topology is easily extracted at the end of the TO process [42,43], and a non-linear analysis (accounting for the non-linear behaviour of the material and for the influence of the contact between the supports of the testing machine and the sample) is performed on the optimised topology for each DC. The goal is to compare the force vs. displacement curve obtained numerically and experimentally to assess the effectiveness of the proposed approach. This represents the first experimental validation of the density-based TO method reformulated in the context of the NURBS entities developed at the I2M laboratory in Bordeaux.

The reminder of the paper is as follows. The problem description and the general work-flow, including numerical and experimental analyses, are introduced in Section 2. Section 3 presents the experimental setup used to characterise the properties of the resin composing the optimised specimens, whilst the fundamentals of the NURBS hyper-surfaces theory and of the SEHM are briefly recalled in Section 4. In Section 5, the mathematical formulation of the multi-scale TO problem is presented in the most general case wherein the topological descriptor is introduced at multiple scales. Section 6 illustrates the numerical results, for each DC, for both 2D and 3D problems. In Section 7, the experimental validation of the optimised topologies through 3PBT is presented together with the non-linear numerical analyses conducted *a posteriori* on the optimised topologies. Finally, Section 8 ends the paper with meaningful conclusions and prospects.

Notation. Upper-case bold letters and symbols are used to indicate tensors (matrices), while lower-case bold letters and symbols indicate column vectors. Subscripts m and M denote quantities evaluated at RVE scale and macroscopic scale, respectively.

2. Problem description

The main goal of this work is the determination of the optimised topology of a structure subject to 3PBT-like BCs with the aim of maximising its flexural stiffness subject to design requirements on lightness and manufacturability. Specifically, three DCs are considered. In the first design case (DC1), the topological variables are defined solely at the macroscopic scale. In the second design case (DC2), the topological descriptor is introduced only at the RVE scale and the loading conditions are imposed at the macroscopic scale. In the third design case (DC3), the topological variables and the design requirements are defined at both lower and upper scales. Of course, in the last two design cases, since the RVE topology is the same at all points of the upper scale domain, the properties of the homogenised material are uniform at the structure-level.

It is noteworthy that in DC3, which is the most general one, unlike the approaches presented in [34–37,44], where the goal is to obtain an optimised topology at the macroscopic scale, by using a pattern of a pre-defined RVE geometry at the lower scale showing a given macroscopic elastic behaviour, in this study, all the problem characteristic scales (i.e., the lower scale and the upper one) are involved in the problem formulation by considering a weak coupling among scales, as discussed in [18]. The work-flow of the approach presented in this study is illustrated in Fig. 1. Particularly, the design strategy is articulated in the following steps:

1. The characterisation of the constitutive law of the material (i.e., the resin) composing the specimens is performed in tension and through 3PBT. From these data, the flexural Young's modulus is calculated and used (together with the Poisson's coefficient) to assess the elasticity tensor of the linear elastic material used in the TO calculations (step 2). Furthermore, the non-linear stress vs. strain curves will be used in the non-linear static analysis (step 5) conducted a-posteriori on each optimised topology.
2. The TO process in the NURBS-density-based framework is conducted for the three design cases discussed above.
3. The boundary of the optimised topology is recovered at the end of the TO process by exploiting the properties of NURBS entities, as explained in [42,43]. Unlike classical density-based TO methods, wherein the pseudo-density field is defined element-wise, the NURBS-density-based method makes use of a pure geometric entity to describe the pseudo-density field at each scale, thus the reconstruction of the boundary of the optimised topology becomes an easy task.
4. The optimised topologies are then converted in suitable standard tessellation language (STL) files. After standard post-processing, they are manufactured through SLA process. Mass evaluation and some geometric measurements are performed to check the conformity of the specimens.
5. 3PBT is conducted by following the procedure detailed in the ASTM norm [41]. The force vs. displacement curve is extracted as a main output of the experimental tests.
6. The boundary of the optimised topology (for each design case) is exported in the ANSYS Workbench® environment and a non-linear static analysis reproducing the BCs of the experimental test is performed, by considering the non-linear behaviour of the bulk material obtained at step 1. The goal is to obtain numerically the force vs. displacement curve.
7. A comparison between experimental and numerical results is performed to assess the accuracy and effectiveness of the proposed approach.

3. Characterisation of the bulk material properties

To assess the behaviour of the Rigid 4000 resin,[1] which is the constitutive material composing the specimens, traction and flexural tests have been carried out on standard samples according to ASTM norms [41,45,46]. The density of this resin is $\rho = 0.0014$ kg m^{-3} and the Poisson's coefficient is $\nu = 0.3$.

3.1. Tensile behaviour of Rigid 4000 resin

According to ASTM D638 norm [46], the tensile Young's modulus and the yield strength[2] (tension) are measured via quasi-static tests performed at a speed equal to 1 mm/min on an INSTRON 5969 machine with a Load Cell of 50 kN.

One type of dog-bone sample is conceived, as shown in Fig. 2, and three specimens are fabricated via SLA technology. By referring to Fig. 2, the nominal dimensions are: LO = 165 mm, WO = 19 mm, $L = 57$ mm, $W = 13$ mm, while the actual value of W and T, measured after manufacturing the specimens, are listed in Table 1.

The load profile chosen to assess yield strength and Young's modulus is a ramp increasing from 0 mm to 5 mm during a time interval equal to $\Delta t = 350$ s. The tensile Young's modulus is extrapolated from the initial region of the $\sigma - \varepsilon$ curves obtained from the test.

The curves resulting from the tensile tests are shown in Fig. 3 and the extrapolated results, in terms of tensile Young's modulus E_t and tensile yield strength σ_{yt}, are listed in Table 2. The resulting $\sigma - \varepsilon$ curve used to describe the tensile behaviour of Rigid 4000 resin is shown

[1] https://formlabs-media.formlabs.com/datasheets/1801088-TDS-FR-0P.pdf.

[2] The notion of yield stress, usually employed for metals, is replaced by the notion of yield strength for polymers but the meaning is the same: it is the value of the stress above which the material begins to deform in a plastic fashion.

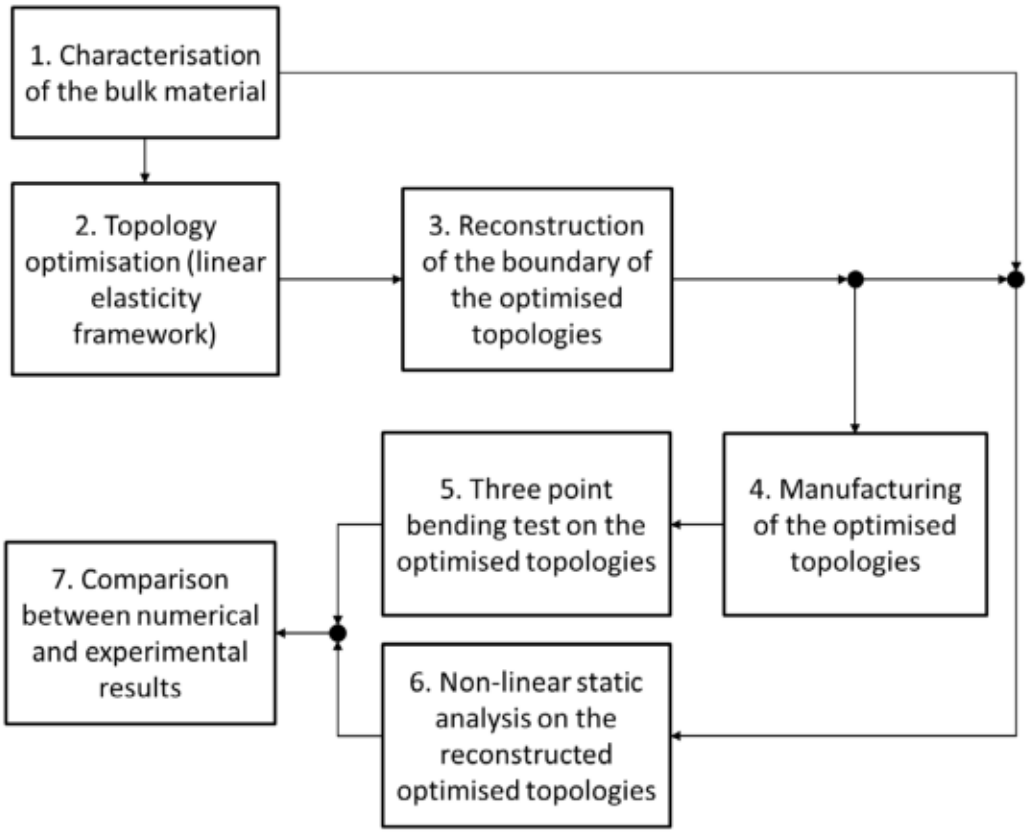

Fig. 1. Work-flow of the design methodology for specimens subject to 3PBT-like loading conditions.

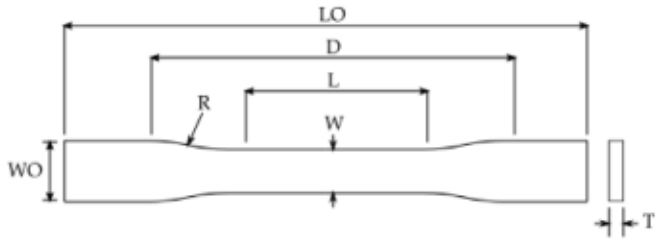

Fig. 2. Schematic representation of the tensile dog-bone-like specimens with the related geometric parameters.

Table 1
Actual values of W and T of the dog-bone samples.

Sample N.	W_{real} [mm]	T_{real} [mm]
1	13.06	3.28
2	13.05	3.3
3	13.01	3.29

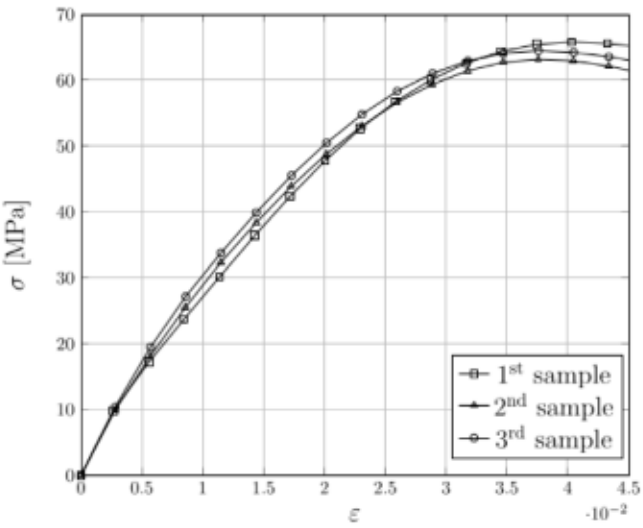

Fig. 3. $\sigma - \varepsilon$ curves obtained from the tensile tests.

in Fig. 4 with the related standard deviation; according to the results shown in Table 2, the tensile Young's modulus is $E_t = 3601.81$ MPa, whilst the tensile yield strength is $\sigma_{yt} = 15.80$ MPa.

3.2. Flexural behaviour of Rigid 4000 resin

To assess the flexural behaviour of the Rigid 4000 resin, the ASTM D790-03 norm [41] is followed. The bending Young's modulus has been extrapolated as a result of the 3PBT conducted via the Adamel Lhomargy DY 36 Load Cell of 100 kN by controlling the displacement with a speed equal to 1 mm/min; particularly, the displacement varies as a ramp in the range $[0, 5.5]$ mm during a time interval equal to

Table 2
Tensile yield strength σ_{yt} and tensile Young's modulus E_t values extrapolated from the results in Fig. 3.

Sample N.	σ_{yt} [MPa]	E_t [MPa]
1	15.60	3536.02
2	15.74	3592.54
3	18.51	3721.93

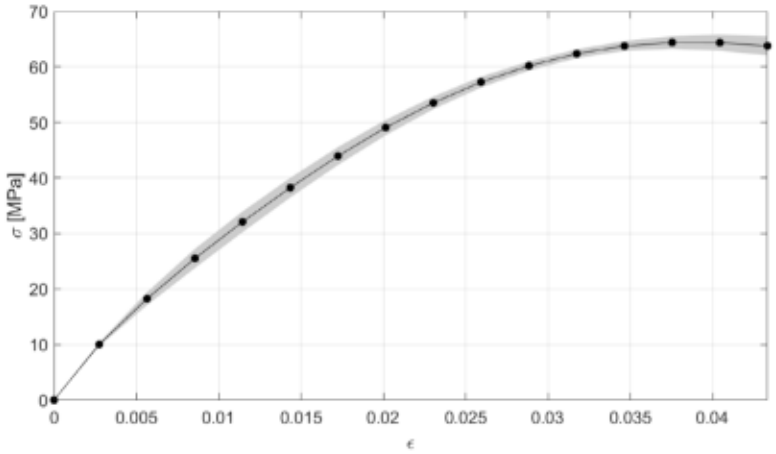

Fig. 4. $\sigma - \varepsilon$ curve of the average tensile material behaviour with the related standard deviation.

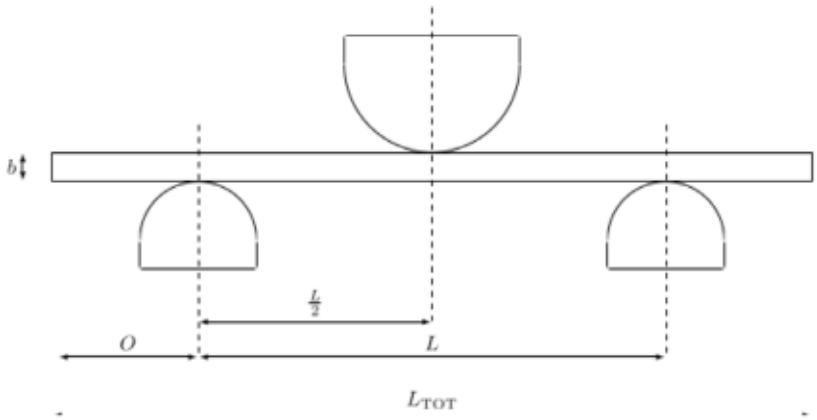

Fig. 5. Schematic representation of the 3PBT apparatus with the related geometric parameters.

$\Delta t = 400$ s. The schematic representation of the experimental apparatus (with the related geometric parameters) is shown in Fig. 5.

Three samples are used during the 3PBT. They are manufactured in the form of a parallelepiped having the following nominal dimension $96 \times 20 \times 5$ mm^3. The flexural Young's modulus E_B is calculated as:

$$E_B = \frac{L^3 m}{4bd^3}, \tag{1}$$

where $L = 80$ mm is the support span, b is the width and d is the depth of the specimen (these geometric parameters are shown in Fig. 5), while m is the slope of the tangent of the force–displacement curve. The values of the actual size of the specimens together with the related values of m and E_B are listed in Table 3.

The resulting $\sigma - \varepsilon$ curve used to describe the flexural behaviour of Rigid 4000 resin is shown in Fig. 6. According to the results shown in Table 3, the flexural Young's modulus is $E_B = 1320.25$ MPa.

4. Theoretical background

4.1. Non-uniform rational basis spline hyper-surfaces

A NURBS hyper-surface is defined as $\mathbf{h} : \mathbb{R}^N \to \mathbb{R}^D$, where N is the dimension of the parametric space, whilst D is the dimension of the co-domain. The formula of a NURBS hyper-surface reads:

$$\mathbf{h}(\zeta_1, \dots, \zeta_N) := \sum_{i_1=0}^{n_1} \cdots \sum_{i_N=0}^{n_N} R_{i_1 \dots i_N}(\zeta_1, \dots, \zeta_N) \mathbf{y}_{i_1, \dots, i_N}, \tag{2}$$

where $R_{i_1 \dots i_N}(\zeta_1, \dots, \zeta_N)$ are the piece-wise rational basis functions related to the standard Bernstein's polynomials $N_{i_k, p_k}(\zeta_k)$, $(k = 1, \dots, N)$

Table 3
Actual dimensions of the samples used for three-point bending test and the related values of m and E_B.

Sample N.	L_{TOT} [mm]	b [mm]	d [mm]	m [N mm^{-1}]	E_B [MPa]
1	96.04	20.12	5.08	27.20	1323.48
2	96.02	20.21	5.09	27.27	1309.84
3	96.01	20.06	5.08	27.27	1327.44

as:

$$R_{i_1 \dots i_N} := \frac{\omega_{i_1 \dots i_N} \prod_{k=1}^{N} N_{i_k, p_k}(\zeta_k)}{\sum_{j_1=0}^{n_1} \cdots \sum_{j_N=0}^{n_N} \left[\omega_{j_1 \dots j_N} \prod_{k=1}^{N} N_{j_k, p_k}(\zeta_k) \right]}. \tag{3}$$

In Eqs. (2) and (3), $\mathbf{h}(\zeta_1, \dots, \zeta_N)$ is a D-dimension vector-valued rational function, $\zeta_k \in [0, 1]$ is the kth dimensionless coordinate (or parametric coordinate), whilst $\mathbf{y}_{i_1, \dots, i_N} \in \mathbb{R}^D$ is the vector collecting the coordinates of the generic control point (CP). The number of CPs along the ζ_j parametric direction is $(n_j + 1)$, with $n_j \in \mathbb{N}$, while $p_j \in \mathbb{N} \cup 0$ $(j = 1, \dots, N)$ is the basis functions degree along the same direction. The jth CP coordinate $y^{(j)}_{i_1, \dots, i_N}$ is stored in the array $\mathbf{Y}^{(j)} \in \mathbb{R}^{(n_1+1) \times \cdots \times (n_N+1)}$, $j = 1, \dots, D$. The explicit expression of CPs coordinates is:

$$\mathbf{Y}^{\mathrm{T}}_{i_1, \dots, i_N} = \{ y^{(1)}_{i_1, \dots, i_N}, \dots, y^{(D)}_{i_1, \dots, i_N} \}. \tag{4}$$

The CPs layout is referred to as *control hyper-net* [47]. The generic CP affects the shape of the NURBS entity by means of its coordinates. The overall number of CPs constituting the hyper-net is:

$$n_{\mathrm{CP}} := \prod_{i=1}^{N} (n_i + 1). \tag{5}$$

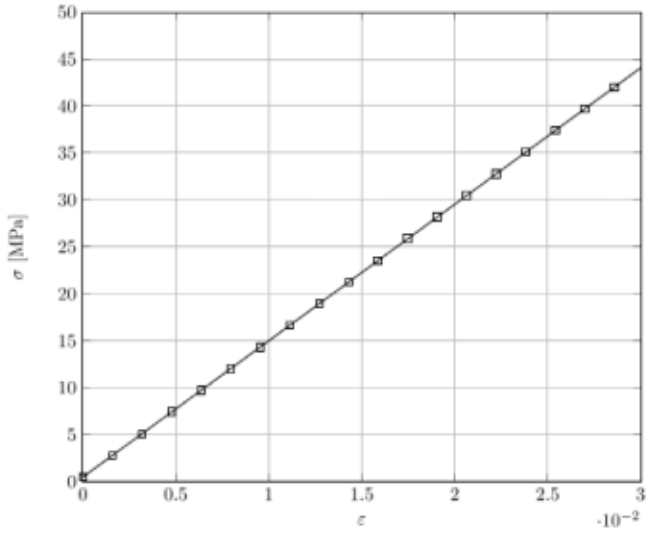

Fig. 6. $\sigma-\varepsilon$ curve of the average flexural material behaviour. The standard deviation is not reported since it takes very small values in the range [0.08–0.21] MPa.

In Eq. (3), a weight $\omega_{i_1\dots i_N}$ is associated to the generic CP. The higher the weight the more the NURBS entity is attracted towards the associated CP. For each parametric direction ζ_k, the NURBS blending functions $N_{i_k,p_k}(\zeta_k)$ appearing in Eq. (3) can be defined recursively as:

$$N_{i_k,0}(\zeta_k) := \begin{cases} 1, \text{ if } v_{i_k}^{(k)} \leq \zeta_k < v_{i_k+1}^{(k)}, \\ 0, \text{ otherwise}, \end{cases} \tag{6}$$

$$N_{i_k,q}(\zeta_k) = \frac{\zeta_k - v_{i_k}^{(k)}}{v_{i_k+q}^{(k)} - v_{i_k}^{(k)}} N_{i_k,q-1}(\zeta_k) + \frac{v_{i_k+q+1}^{(k)} - \zeta_k}{v_{i_k+q+1}^{(k)} - v_{i_k+1}^{(k)}} N_{i_k+1,q-1}(\zeta_k), \tag{7}$$
$$q = 1, \dots, p_k, \;\; k = 1, \dots, N,$$

where each constitutive blending function is defined on the knot vector:

$$\mathbf{v}_{(k)}^{\mathrm{T}} = \{\underbrace{0, \dots, 0}_{p_k+1}, v_{p_k+1}^{(k)}, \dots, v_{m_k-p_k-1}^{(k)}, \underbrace{1, \dots, 1}_{p_k+1}\}, \tag{8}$$
$$\mathbf{v}_{(k)} \in \mathbb{R}^{m_k+1}, \;\; k = 1, \dots, N,$$

with:

$$m_k = n_k + p_k + 1. \tag{9}$$

The NURBS blending functions are characterised by several interesting properties: the reader is addressed to [47] for more details on the topic. Here, only the *local support property* is recalled because it is exploited in the context of the NURBS-density-based method [38–40]:

$$R_{i_1\dots i_N}(\zeta_1, \dots, \zeta_N) \neq 0,$$
$$\text{if } (\zeta_1, \dots, \zeta_N) \in \left[v_{i_1}^{(1)}, v_{i_1+p_1+1}^{(1)}\right[\times \cdots \times \left[v_{i_N}^{(N)}, v_{i_N+p_N+1}^{(N)}\right[. \tag{10}$$

Eq. (10) implies that each CP (and the associated weight) affects only a precise zone of the parametric space, which is denoted as *local support*.

4.2. The strain energy-based homogenisation method

When dealing with the design of ACMs at multiple scales, a homogenisation procedure is mandatory to set the transition among the scales of the problem at hand. At the lower scale, the RVE of the ACM can be interpreted, from a mechanical standpoint, as a heterogeneous medium composed of two constituents, i.e., the bulk material and the void. At the macroscopic scale, instead, it is modelled as an equivalent homogeneous anisotropic medium whose mechanical response is described by a set of equivalent material properties. Accordingly, the macroscopic structural responses will depend upon both the topological descriptor defined at the RVE scale (through the calculation of the equivalent material properties of the homogenised continuum) and the one introduced at the macroscopic scale to describe the distribution of the equivalent homogeneous material (see Section 5 for more details on the definition of the topological variable at each scale).

To assess the macroscopic structural responses and their dependency upon the topological variable introduced at the lower scale, in this study, the macroscopic elastic behaviour of the RVE is determined using the SEHM of periodic media [48]. It is noteworthy that two variants of the SEHM are available in the literature: the first one makes use of the elements averaged stresses to compute the components of the macroscopic elasticity matrix $\mathbf{C}_M$ [48], whilst the second one employs the strain energy of the elements to determine $\mathbf{C}_M$ [6]. As discussed in [6], the SEHM based on the strain energy of elements requires the least number of finite element (FE) analyses to compute the components of $\mathbf{C}_M$ (and the related gradient with respect to the topological variable defined at the RVE scale). Accordingly, only this variant is used in the following to set the scale transition.

The SEHM technique makes use of the repetitive unit of the ACM to evaluate the resulting macroscopic physical properties. The basic feature of the SEHM is the assumption that the strain energy of the RVE of the ACM and the one of the corresponding volume of the homogeneous solid at the macroscopic scale are equal. To evaluate the elastic response of the ACM at the macroscopic scale, two main hypotheses are considered: (a) linear, elastic behaviour for the constitutive material of the RVE; (b) the buckling of the ACM topological branches is disregarded.

To determine the stiffness tensor $\mathbf{C}_M$ of the ACM at the macroscopic scale, the RVE is submitted to an average strain field ε_{ij}^0, $i,j = 1,2,3$ (tensor notation). The six independent components of the average strain tensor are applied through the following set of periodic BCs on the RVE faces [48]:

$$\begin{cases} u_{mi}(2a_{m1}, x_{m2}, x_{m3}) - u_{mi}(0, x_{m2}, x_{m3}) = 2a_{m1}\varepsilon_{mi1}^0, \\ \qquad (0 \leq x_{m2} \leq 2a_{m2}, \;\; 0 \leq x_{m3} \leq 2a_{m3}), \\ u_{mi}(x_{m1}, 2a_{m2}, x_{m3}) - u_{mi}(x_{m1}, 0, x_{m3}) = 2a_{m2}\varepsilon_{mi2}^0, \\ \qquad (0 \leq x_{m1} \leq 2a_{m1}, \;\; 0 \leq x_{m3} \leq 2a_{m3}), \\ u_{mi}(x_{m1}, x_{m2}, 2a_{m3}) - u_{mi}(x_{m1}, x_{m2}, 0) = 2a_{m3}\varepsilon_{mi3}^0, \\ \qquad (0 \leq x_{m1} \leq 2a_{m1}, \;\; 0 \leq x_{m2} \leq 2a_{m2}), \end{cases} \tag{11}$$

where $i = 1,2,3$. In the above equations, $L_{mi} = 2a_{mi}$ is the characteristic length of the RVE along the x_{mi} axis, while u_{mi} is the component of the displacement field along the same axis.

Consider the equilibrium equation of the FE model of the RVE. In the most general case it reads:

$$\hat{\mathbf{K}}_m \hat{\mathbf{u}}_m = \hat{\mathbf{f}}_m,$$
$$\hat{\mathbf{u}}_m, \hat{\mathbf{f}}_m \in \mathbb{R}^{\hat{N}_{m\mathrm{DOF}}}, \;\; \hat{\mathbf{K}}_m \in \mathbb{R}^{\hat{N}_{m\mathrm{DOF}} \times \hat{N}_{m\mathrm{DOF}}}, \tag{12}$$

where $\hat{N}_{m\mathrm{DOF}}$ is the overall number of degrees of freedom (DOFs) of the structure before the application of the BCs, while $\hat{\mathbf{K}}_m$ is the non-reduced (singular) stiffness matrix of the RVE. $\hat{\mathbf{u}}_m$ is the non-reduced vector of generalised displacements containing both imposed and unknown DOFs of the FE model and $\hat{\mathbf{f}}_m$ is the non-reduced vector of generalised nodal forces (both known and unknown quantities). The expression of the above vectors and matrix is:

$$\hat{\mathbf{K}}_m := \begin{bmatrix} \mathbf{K}_m & \mathbf{K}_{m\mathrm{BC}} \\ \mathbf{K}_{m\mathrm{BC}}^{\mathrm{T}} & \tilde{\mathbf{K}}_m \end{bmatrix}, \;\; \hat{\mathbf{u}}_m := \begin{Bmatrix} \mathbf{u}_m \\ \mathbf{u}_{m\mathrm{BC}} \end{Bmatrix}, \;\; \hat{\mathbf{f}}_m := \begin{Bmatrix} \mathbf{f}_m \\ \mathbf{r}_m \end{Bmatrix}, \tag{13}$$
$$\mathbf{u}_m, \;\; \mathbf{f}_m \in \mathbb{R}^{N_{m\mathrm{DOF}}}, \;\; \mathbf{u}_{m\mathrm{BC}}, \;\; \mathbf{r}_m \in \mathbb{R}^{N_{m\mathrm{BC}}},$$
$$\mathbf{K}_m \in \mathbb{R}^{N_{m\mathrm{DOF}} \times N_{m\mathrm{DOF}}}, \mathbf{K}_{m\mathrm{BC}} \in \mathbb{R}^{N_{m\mathrm{DOF}} \times N_{m\mathrm{BC}}}, \;\; \tilde{\mathbf{K}}_m \in \mathbb{R}^{N_{m\mathrm{BC}} \times N_{m\mathrm{BC}}}.$$

In Eq. (13), $N_{m\mathrm{DOF}}$ is the number of unknown DOFs, while $N_{m\mathrm{BC}}$ represents the number of DOFs where BCs on generalised displacements are applied (of course $\hat{N}_{m\mathrm{DOF}} = N_{m\mathrm{DOF}} + N_{m\mathrm{BC}}$). $\mathbf{u}_m$ and $\mathbf{u}_{m\mathrm{BC}}$ are

the unknown and known vectors of generalised displacements, respectively. $\mathbf{f}_m$ is the vector of generalised external nodal forces, whilst $\mathbf{r}_m$ is the vector of generalised nodal reactions where BCs on generalised displacements are imposed. $\mathbf{K}_m$, $\mathbf{K}_{m\mathrm{BC}}$ and $\tilde{\mathbf{K}}_m$ are the stiffness matrices of the FE model of the RVE after applying BCs. Since periodic BCs of Eq. (11) are imposed in terms of displacements and no external forces are applied to the FE model of the RVE, i.e., $\mathbf{f}_m = \mathbf{0}$, the equilibrium problem of Eq. (13) is of the Dirichlet's type.

By considering elementary (i.e., uni-axial and bi-axial) strain components in Eq. (11), and by imposing the equivalence between the strain energy of the equivalent homogeneous anisotropic continuum and that of the RVE of the ACM, the components of tensor $\mathbf{C}_M$ (Voigt's notation) can be determined as [6]:

$$C_{Mkk} = \frac{\mathcal{W}_m\left(\varepsilon^0_{mk}\right)}{V_{\mathrm{RVE}}\left(\varepsilon^0_{mk}\right)^2}, \quad k = 1, \ldots, 6, \tag{14}$$

$$C_{Mij} = \frac{\mathcal{W}_m\left(\varepsilon^0_{mi}, \varepsilon^0_{mj}\right)}{2V_{\mathrm{RVE}}\varepsilon^0_{mi}\varepsilon^0_{mj}} - C_{Mii}\frac{\varepsilon^0_{mi}}{2\varepsilon^0_{mj}} - C_{Mjj}\frac{\varepsilon^0_{mj}}{2\varepsilon^0_{mi}}, \quad i, j = 1, \ldots, 6,\ i \neq j. \tag{15}$$

Eq. (14) is used to evaluate the terms belonging to the main diagonal of tensor $\mathbf{C}_M$, whilst Eq. (15) allows for determining the terms outside the main diagonal. $\mathcal{W}_m\left(\varepsilon^0_{mk}\right)$ and $\mathcal{W}_m\left(\varepsilon^0_{mi}, \varepsilon^0_{mj}\right)$ represent the work of internal forces, evaluated for uni-axial and bi-axial strain fields, respectively, while $V_{\mathrm{RVE}} = 8a_{m1}a_{m2}a_{m3}$ is the volume of the design domain of the RVE in the case of 3D problems. It is noteworthy that Eq. (14) must be solved before Eq. (15): in the most general case, i.e., for a macroscopic anisotropic behaviour, six static analyses must be solved for 3D problems to calculate the diagonal terms of the stiffness tensor and to deduce the extra diagonal terms via the superposition principle; see [6] for more details on this topic.

5. Multi-scale topology optimisation: the NURBS-density-based method

As stated in Section 2, the goal of this study is to determine the optimal topology of the continuum (at each characteristic scale of the problem at hand), which minimises the generalised compliance [40] by meeting the following design requirements:

1. A constraint on the mass fraction imposed at the upper scale.
2. A constraint on the volume fraction imposed to the topological descriptor defined at the lower scale (this constraint is introduced only for DC3).
3. A constraint on the minimum thickness that can be fabricated through the SLA process. This constraint is formulated as a minimum member size constraint at the structure scale or at the RVE scale, depending on the problem formulation.
4. When the topological descriptor is defined at both lower and upper scales (DC3), a constraint on the scale separation condition is introduced to ensure the validity of the results of the homogenisation technique in calculating equivalent elastic properties of the material at the upper scale, according to the strategy discussed in [18]. Since the topology of the RVE and the one of the structure are continuously changing during the optimisation process, introducing this type of constraint is of capital importance to avoid the occurrence of too small topological branches at the upper scale whose size could become of the same order of magnitude of the RVE characteristic length (in such circumstances the results of the homogenisation technique are not correct). Specifically, the smallest thickness of the topological branches occurring at the upper scale must be greater than or equal to a multiple of the characteristic length of the design domain at the lower scale.

For the sake of brevity, the problem formulation is presented only for the most general case (DC3): in this case the goal is to determine the optimised topology of the ACM at both RVE scale and macroscopic scale. This problem can also be interpreted as a design problem of a complex anisotropic medium whose goal is the concurrent optimisation of the material properties (performed through the optimisation of the RVE topology at the lower scale) and of the macroscopic topology (i.e., the distribution of the equivalent homogeneous anisotropic material at the upper scale). Since the RVE topology is the same at all points of the upper scale domain, the properties of the homogenised material are uniform at this scale.

Remark 5.1. In this study, the characteristic scales of the problem are weakly coupled, which means that the design requirements calculated at the macroscopic scale (and involved in the problem formulation) depend upon the topological variables defined at both scales. On the one hand, quantities describing the behaviour of the RVE at the upper scale (e.g., the equivalent elastic properties of the homogeneous anisotropic material replacing the RVE, the volume fraction of the RVE, etc.) depend only upon the topological descriptor defined at the RVE scale. On the other hand, the structural responses defined at the macroscopic scale (e.g., the compliance, the displacement field, etc.) depend upon the topological descriptors defined at both scales. Of course, the dependency of the macroscopic structural responses upon the topological descriptor defined at the lower scale is implicit because the RVE topology affects the components of the macroscopic elasticity matrix $\mathbf{C}_M$.

Remark 5.2. The notion of scale separation introduced in this work is the one ensuring the validity of the results of the homogenisation process at the upper scale within a continuously changing topology. This concept should not be confused with the notion of coupling between scales. The scales are separated only in terms of characteristic lengths, but they are coupled because the structural responses at the upper scale depend upon the geometrical and material parameters defined at the lower scale. More details on this aspect are available in [18].

The main features of the approach are briefly described here only for 3D multi-scale TO problems. The characteristic scales of the problem (and the relative geometrical features) are illustrated in Fig. 7 in the most general case (DC3).

5.1. Design variables

Consider the compact Euclidean space $D_\chi \subset \mathbb{R}^3$, defining the design domain at the generic χth scale ($\chi = m, M$), in a Cartesian orthogonal frame $\mathrm{O}(x_{\chi 1}, x_{\chi 2}, x_{\chi 3})$:

$$D_\chi := \{\mathbf{x}^{\mathrm{T}}_\chi = \left(x_{\chi 1}, x_{\chi 2}, x_{\chi 3}\right) \in \mathbb{R}^3 : x_{\chi j} \in [0, L_{\chi j}],\ j = 1, 2, 3\},\quad \chi = m, M, \tag{16}$$

where $L_{\chi j}$ is the characteristic length of the domain defined along $x_{\chi j}$ axis, as shown in Fig. 7. In the density-based TO approach, the *material domain* $\Omega_\chi \subseteq D_\chi$ at the generic scale is identified by means of the pseudo-density function $\rho_\chi(\mathbf{x}_\chi) \in [0, 1]$ for $\mathbf{x}_\chi \in D_\chi$: $\rho_\chi(\mathbf{x}_\chi) = 0$ means absence of material, whilst $\rho_\chi(\mathbf{x}_\chi) = 1$ implies presence of material. The number and the type of design variables depend, of course, upon the characteristic scales involved in the problem at hand. Particularly, three design cases are considered in this work: (a) the topological descriptor is defined only at the macroscopic scale (DC1), hence $\chi = M$; (b) the topological descriptor is defined only at the RVE scale (DC2), thus $\chi = m$; (c) the topological descriptor is defined at both scales (DC3), hence $\chi = m, M$.

In the framework of the NURBS-density-based method, the topological variable (at each scale) is represented by a NURBS entity. Specifically, a NURBS entity of dimension $D + 1$ is used to describe the pseudo-density field, i.e., the topological variable, of a problem

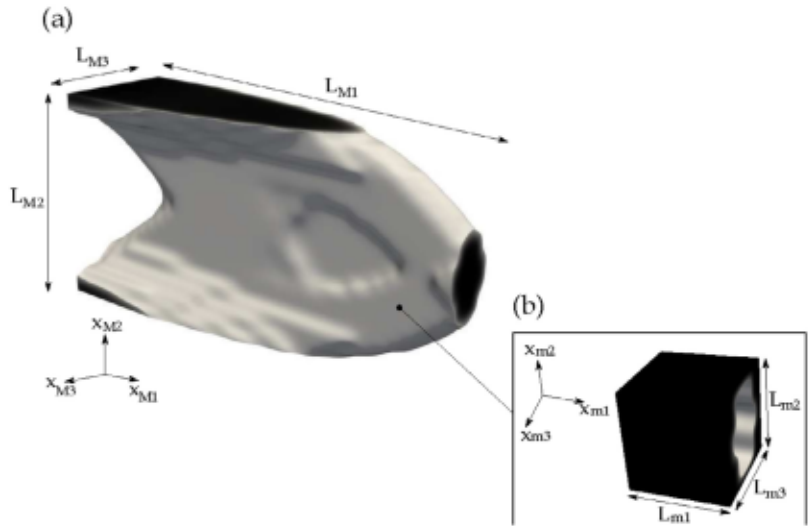

Fig. 7. Characteristic scales of the two-scale topology optimisation problem: (a) the upper scale of the structure and (b) the lower scale of the representative volume element of the architected cellular material.

of dimension D. Therefore, for a 3D TO problem a 4D NURBS hyper-surface is needed to describe the part topology [39,40]. The first three coordinates of the hyper-surface correspond to the Cartesian coordinates defining the domain, while the last coordinate corresponds to the pseudo-density field that reads:

$$\rho_\chi(\zeta_{\chi 1},\zeta_{\chi 2},\zeta_{\chi 3}) = \sum_{i_{\chi 1}=0}^{n_{\chi 1}} \sum_{i_{\chi 2}=0}^{n_{\chi 2}} \sum_{i_{\chi 3}=0}^{n_{\chi 3}} R_{i_{\chi 1} i_{\chi 2} i_{\chi 3}}(\zeta_{\chi 1},\zeta_{\chi 2},\zeta_{\chi 1}) \rho_{\chi i_{\chi 1} i_{\chi 2} i_{\chi 3}}, \quad \chi = m, M, \tag{17}$$

where $\rho_{\chi i_{\chi 1} i_{\chi 2} i_{\chi 3}}$ is the pseudo-density value at the generic CP, while $R_{i_{\chi 1} i_{\chi 2} i_{\chi 3}}$ are the rational basis functions of Eq. (3). The dimensionless parameters $\zeta_{\chi j}$ can be obtained as:

$$\zeta_{\chi j} = \frac{x_{\chi j}}{L_{\chi j}}, \quad \chi = m, M, \quad j = 1, 2, 3. \tag{18}$$

Among the parameters governing the shape of the NURBS entity, only the pseudo-density at CPs and the associated weights are included in the design variable vectors $\boldsymbol{\xi}_{\chi 1}$ and $\boldsymbol{\xi}_{\chi 2}$ defined as:

$$\boldsymbol{\xi}_{\chi 1}^{\mathrm{T}} := \left(\rho_{000}, \ldots, \rho_{n_{\chi 1} n_{\chi 2} n_{\chi 3}}\right), \ \boldsymbol{\xi}_{\chi 2}^{\mathrm{T}} := \left(\omega_{000}, \ldots, \omega_{n_{\chi 1} n_{\chi 2} n_{\chi 3}}\right), \quad \boldsymbol{\xi}_{\chi 1}, \boldsymbol{\xi}_{\chi 2} \in \mathbb{R}^{n_{\chi \mathrm{CP}}}, \tag{19}$$

accordingly, the number of design variables for each scale is, at most, $n_{\chi \mathrm{var}} = 2n_{\chi \mathrm{CP}}$, $\chi = m, M$. The other parameters involved in the definition of the NURBS entity, i.e., degrees, knot-vector components and number of CPs, are set a-priori at the beginning of the TO and are not optimised: for more details the reader is addressed to [39,40].

5.2. Objective function

At the lower scale, the stiffness matrix of the FE model of the RVE is penalised as follows:

$$\hat{\mathbf{K}}_m := \sum_{e=1}^{N_{me}} \rho_{me}^{\alpha}\left(\xi_{m1}, \xi_{m2}\right) \hat{\mathbf{L}}_{me}^{\mathrm{T}} \mathbf{K}_{me} \hat{\mathbf{L}}_{me}, \tag{20}$$

where ρ_{me} is the fictitious density of Eq. (17) computed at the centroid of the generic element e and N_{me} is the total number of elements composing the FE model of the RVE. $\hat{\mathbf{L}}_{me} \in \mathbb{R}^{N_{m\mathrm{DOF}}^e \times \hat{N}_{m\mathrm{DOF}}}$ is the connectivity matrix of element e (whose number of DOFs is $N_{m\mathrm{DOF}}^e$), whilst $\mathbf{K}_{me} \in \mathbb{R}^{N_{m\mathrm{DOF}}^e \times N_{m\mathrm{DOF}}^e}$ is the non-penalised element stiffness matrix expressed in the global reference frame of the model. In Eq. (20), $\alpha \geq 1$ is a suitable parameter that aims at penalising all the meaningless densities between 0 and 1: in agreement with the classic SIMP approach this parameter is set as $\alpha = 3$.

The pseudo-density function defined at the lower scale affects also the mechanical performances of the structure at the upper scale via the elasticity tensor $\mathbf{C}_M$, according to Eqs. (14) and (15). Indeed, the elasticity tensor of the equivalent homogeneous anisotropic material is involved in the definition of the global stiffness matrix of the FE model at the macroscopic scale $\hat{\mathbf{K}}_M$. Accordingly, matrix $\hat{\mathbf{K}}_M$ depends upon the pseudo-density fields defined at both scales as follows:

$$\hat{\mathbf{K}}_M := \sum_{e=1}^{N_{Me}} \rho_{Me}^{\alpha}\left(\xi_{M1}, \xi_{M2}\right) \hat{\mathbf{L}}_{Me}^{\mathrm{T}} \int_{\Omega_{Me}} \mathbf{B}_{Me}^{\mathrm{T}} \mathbf{C}_M \left(\xi_{m1}, \xi_{m2}\right) \mathbf{B}_{Me} d\Omega \hat{\mathbf{L}}_{Me}, \tag{21}$$

where N_{Me} is the number of elements constituting the FE model at the upper scale, ρ_{Me} is the fictitious density of Eq. (17) computed at the centroid of the generic element e of the FE model at upper scale, $\hat{\mathbf{L}}_{Me} \in \mathbb{R}^{N_{M\mathrm{DOF}}^e \times \hat{N}_{M\mathrm{DOF}}}$ is the connectivity matrix of element e (whose number of DOFs is $N_{M\mathrm{DOF}}^e$), while $\mathbf{B}_{Me} \in \mathbb{R}^{6 \times N_{M\mathrm{DOF}}^e}$ is the matrix representing the product between the linear differential operator and the shape function matrices of the generic element.

The formulation of the equilibrium problem for a linear static analysis, considering the most general case of inhomogeneous Neumann–Dirichlet BCs, reads:

$$\hat{\mathbf{K}}_M \hat{\mathbf{u}}_M = \hat{\mathbf{f}}_M, \quad \hat{\mathbf{u}}_M, \hat{\mathbf{f}}_M \in \mathbb{R}^{\hat{N}_{M\mathrm{DOF}}}, \hat{\mathbf{K}}_M \in \mathbb{R}^{\hat{N}_{M\mathrm{DOF}} \times \hat{N}_{M\mathrm{DOF}}}, \tag{22}$$

where $\hat{N}_{M\mathrm{DOF}}$ is the overall number of DOFs of the FE model at the macroscopic scale, whilst $\hat{\mathbf{u}}_M$ and $\hat{\mathbf{f}}_M$ are the non-reduced vectors of generalised displacements and forces, respectively. In analogy with Eq. (13), Eq. (22) can be rewritten as follows:

$$\begin{bmatrix} \mathbf{K}_M & \mathbf{K}_{M\mathrm{BC}} \\ \mathbf{K}_{M\mathrm{BC}}{}^{\mathrm{T}} & \bar{\mathbf{K}}_M \end{bmatrix} \begin{Bmatrix} \mathbf{u}_M \\ \mathbf{u}_{M\mathrm{BC}} \end{Bmatrix} = \begin{Bmatrix} \mathbf{f}_M \\ \mathbf{r}_M \end{Bmatrix}$$
$$\mathbf{u}_M, \ \mathbf{f}_M \in \mathbb{R}^{N_{M\mathrm{DOF}}}, \ \mathbf{u}_{M\mathrm{BC}}, \ \mathbf{r}_M \in \mathbb{R}^{N_{M\mathrm{BC}}},$$
$$\mathbf{K}_M \in \mathbb{R}^{N_{M\mathrm{DOF}} \times N_{M\mathrm{DOF}}}, \mathbf{K}_{M\mathrm{BC}} \in \mathbb{R}^{N_{M\mathrm{DOF}} \times N_{M\mathrm{BC}}}, \ \bar{\mathbf{K}}_M \in \mathbb{R}^{N_{M\mathrm{BC}} \times N_{M\mathrm{BC}}}, \tag{23}$$

where the physical meaning of the different quantities is the same as the counterparts defined at the lower scale, see Section 4.2. As discussed in [40], under inhomogeneous Neumann–Dirichlet BCs, the generalised compliance C_M at the upper scale is defined as:

$$C_M := \mathbf{f}_M^{\mathrm{T}} \mathbf{u}_M - \mathbf{r}_M^{\mathrm{T}} \mathbf{u}_{M\mathrm{BC}}. \tag{24}$$

Since in this study the continuum is submitted to 3PBT-like BCs at the upper scale, and since the 3PBT is performed by controlling the imposed displacement, only inhomogeneous BCs of the Dirichlet's type must be considered in Eq. (24), i.e., $\mathbf{u}_{MBC} \neq \mathbf{0}$ and $\mathbf{f}_M = \mathbf{0}$. Accordingly, the generalised compliance simplifies to:

$$C_M = -\mathbf{r}_M^{\mathrm{T}} \mathbf{u}_{MBC}. \tag{25}$$

Therefore, the generalised compliance is a non-positive definite functional in the case of the 3PBT.

Inasmuch as the solution search for the multi-scale TO problem is performed via a deterministic algorithm, the derivation of the formal expression of the gradient of the objective function with respect to the topological variable introduced at each scale (and of the constraint functions too) is needed to speed up the optimisation process. Such expressions were derived in previous works [6,40] and are reported in Appendix for the sake of completeness.

5.3. Constraint functions

The design requirements, which are integrated in the problem formulation as optimisation constraints, are presented in the following. The first requirement is related to the lightness of the structure and is formulated in terms of a constraint on the overall mass of the structure m_M. The mass of the structure reads:

$$m_M = \tau_M V_M, \tag{26}$$

with

$$V_M = \sum_{e=1}^{N_{Me}} \rho_{Me} V_{Me}. \tag{27}$$

In Eq. (27), V_{Me} is the volume of the generic element composing the mesh of the FE model at the upper scale. In Eq. (26), τ_M is the density of the equivalent homogeneous anisotropic medium which is defined as:

$$\tau_M := \frac{\tau_m}{V_{\mathrm{RVE}}} \sum_{e=1}^{N_{me}} \rho_{me} V_{me}, \tag{28}$$

where $\tau_m = \rho$ is the density of the constitutive material composing the RVE of the ACM and V_{me} is the volume of the generic element composing the FE model of the RVE. Therefore, the lightness requirement is formulated as:

$$g_1(\xi_{M1}, \xi_{M2}, \xi_{m1}, \xi_{m2}) := \frac{m_M}{m_{M\mathrm{ref}}} - \gamma_{Mm} \leq 0, \tag{29}$$

In the above formula, $m_{M\mathrm{ref}}$ is the reference value of the macroscopic mass, whilst γ_{Mm} is the imposed mass fraction. A further requirement is considered in terms of the volume fraction of the solid phase at the RVE scale when DC3 is considered. To this end, the RVE volume is introduced as:

$$V_m := \sum_{e=1}^{N_{me}} \rho_{me} V_{me}. \tag{30}$$

Accordingly, the requirement on the volume fraction of the RVE solid phase is expressed as:

$$g_2(\xi_{m1}, \xi_{m2}) := \frac{V_m}{V_{\mathrm{RVE}}} - \gamma_{mV} \leq 0, \tag{31}$$

where γ_{mV} is the imposed volume fraction.

As stated above, two further requirements are included in the problem formulation. The first one deals with the scale separation condition if the topological descriptor is defined at both lower and upper scales (DC3). As discussed in [18], this requirement is introduced through a minimum length scale condition on the topological variable at the upper scale. Specifically, to ensures the validity of the results of the SEHM, the minimum size of the topological branches at the upper scale must be greater than or equal to a multiple of the characteristic size of the RVE at the lower scale. The second requirement is a technological constraint related to the minimum printable size and it is introduced as a minimum member size constraint at the lower scale (DC2 and DC3) or upper scale (DC1), depending on the problem formulation.

The main advantages of the NURBS-density-based method are recalled here below.

- The topological descriptor, i.e., the pseudo-density field, at the generic scale, for a problem of dimension D is described through a geometric entity of dimension $D + 1$, i.e., the NURBS hyper-surface.
- Unlike the classic density-based TO method, wherein the pseudo-density field is defined element-wise, thanks to the local support property of the NURBS basis functions, the NURBS-density-based method does not require the introduction of artificial filtering techniques to avoid checker-board effect and to avoid/reduce the dependency of the optimised topology to the mesh quality. Particularly, the optimised topology (at the generic scale) does not depend about the size of the elements composing the mesh of the FE model (at that scale), but depends, of course, upon the integer parameters tuning the size of the local support, i.e., degrees of the Bernstein's polynomials and number of CPs [49]. This means that an eventual mesh refinement has an impact only on the value of the structural responses (displacements, strains, stresses, etc.), but not on the minimum member size of the topology.
- Fig. 8 illustrates one of the main advantages of the NURBS-density-based method: the possibility of exporting a CAD-compatible entity to any CAD software. This allows for an easy reconstruction of the boundary of the optimised topology for 2D problems. Conversely, for 3D problems, wherein a 4D NURBS hyper-surface is used to represent the topology, the process is more elaborate because it requires the formulation of a dedicated surface fitting problem as discussed in [42]. Regardless of the problem dimension, the boundary of the optimised topology is available at each iteration (thus geometric constraints related to the properties of the boundary can be imposed in a relatively easy way) and can be retrieved straightforwardly by evaluating the threshold value for the density field meeting the optimisation constraints (this operation is automatically done by the algorithm at the end of the optimisation process).
- A further advantage of the NURBS-density-based method is in the handling of the geometric constraints imposed on the topological variable at the generic scale, as widely discussed in [49]. Specifically, since the pseudo-density field describing the topology of the continuum, at both scales, is described through a NURBS hyper-surface, it is possible to set the integer parameters (number of CPs and basis functions degree along each parametric direction) governing its shape to automatically satisfy the minimum length scale requirement, without introducing an explicit optimisation constraint in the problem formulation. Therefore, according to the guidelines provided in [18,49], the scale separation requirement and the manufacturing requirement are controlled by means of this feature.

More details on the reconstruction strategy and on the advantages of the NURBS-density-based algorithm are available in [38,39,42].

5.4. Problem formulation

Here below, the problem formulation is reported for the most general case, wherein the topological descriptors are introduced at both lower and upper scales [18]. Accordingly, the multi-scale TO problem is formulated as a constrained non-linear programming problem (CNLPP)

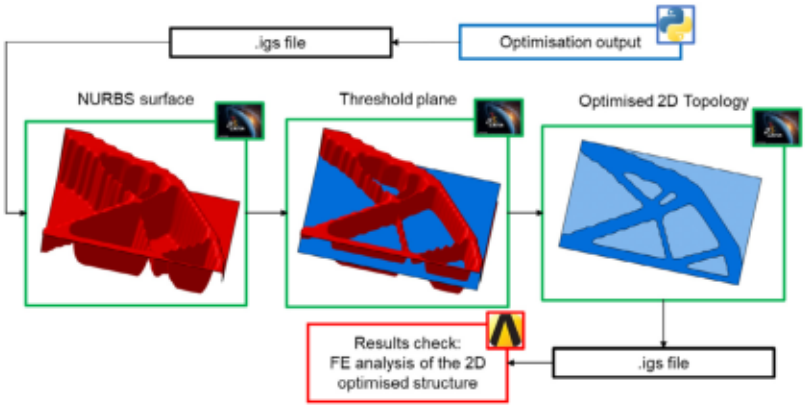

Fig. 8. Main steps of the reconstruction of the boundary of the optimised topology for 2D problems in the framework of the NURBS-density-based method.

Table 4
GCMMA algorithm parameters.

Parameter	Value
move	0.1
albefa	0.1
Stop criterion	**Value**
Maximum n. of function evaluations	10 000
Maximum n. of iterations	$20 \times n_{var}$
Tolerance on objective function	10^{-6}
Tolerance on constraints	10^{-6}
Tolerance on input variables change	10^{-6}
Tolerance on Karush –Kuhn –Tucker norm	10^{-6}

as follows:

$$\min_{\xi_{\tau 1},\xi_{\tau 2}} \frac{C_M}{|C_{M\mathrm{ref}}|}, \text{ s.t. : } \begin{cases} \hat{\mathbf{K}}_\tau \hat{\mathbf{u}}_\tau = \hat{\mathbf{f}}_\tau, \\ g_1(\xi_{M1},\xi_{M2},\xi_{m1},\xi_{m2}) \le 0, \\ g_2(\xi_{m1},\xi_{m2}) \le 0, \\ \xi_{\tau 1 k_\tau} \in [\rho_{\tau\min},\rho_{\tau\max}], \quad \xi_{\tau 2 k_\tau} \in [\omega_{\tau\min},\omega_{\tau\max}], \\ \tau = m, M, \ \forall k_\tau = 1,\dots,n_{\tau\mathrm{CP}}. \end{cases} \tag{32}$$

Of course, the number and the type of constraint functions as well as the number of design variables involved in the problem formulation depend upon the DC at hand, as discussed in Section 2. Particularly, in Eq. (32), the design requirement g_1 is always active, whilst g_2 is active only when the topological descriptor is introduced at the both macroscopic scale and RVE scale (DC3). Moreover, in Eq. (32), $C_{M\mathrm{ref}}$ is the reference value of the macroscopic compliance, whilst $\rho_{\tau\min}$ and $\rho_{\tau\max}$ are lower and upper bounds on the pseudo-density at each CP, and $\omega_{\tau\min}$ and $\omega_{\tau\max}$ are the bounds on the generic weight (the bounds on the design variables are introduced at each characteristic scale). The overall number of design variables of problem (32) depends upon the DC at hand and it is equal to: (a) $n_{\mathrm{var}} = 2n_{MCP}$ for DC1; (b) $n_{\mathrm{var}} = 2n_{m\mathrm{CP}}$ for DC2; (c) $n_{\mathrm{var}} = 2n_{m\mathrm{CP}} + 2n_{MCP}$ for DC3.

6. Numerical results

The proposed methodology is tested on both 2D and 3D problems: all calculations are carried out by means of the code SANTO (SIMP and NURBS for topology optimisation). The software, coded in python language, is interfaced with the FE code ANSYS® to compute the mechanical responses of the structure at each scale. Moreover, the CNLPP of Eq. (32) has been solved through the globally-convergent method of moving asymptotes (GCMMA) algorithm [50], whose parameters are listed in Table 4.

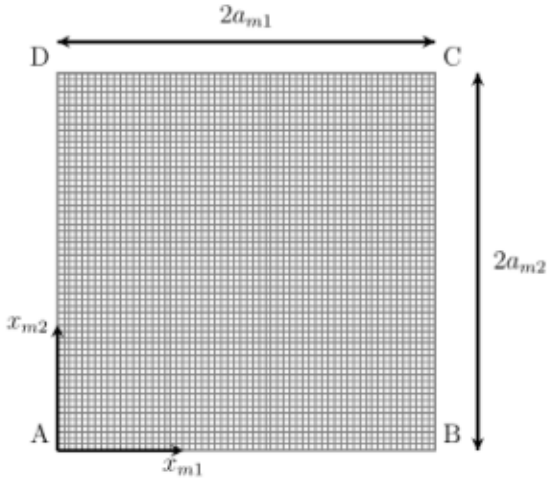

Fig. 9. Finite element model of the representative volume element with its characteristic size for 2D problems.

The design variables bounds are set as follows: $\rho_{\chi\min} = 10^{-3}$, $\rho_{\chi\max} = 1$; $\omega_{\chi\min} = 0.5$, $\omega_{\chi\max} = 10$ ($\chi = m, M$). Regarding the other continuous parameters involved in the NURBS entity definition in the 2D and 3D cases, the non-trivial knot vectors components in Eq. (8) are evenly distributed in the interval $]0,1[$.

Furthermore, symmetry constraints are imposed to the pseudo-density field describing the RVE topology: double symmetry for 2D problems (with respect to axes $x_{mj} = a_{mj}$, $j = 1,2$) and three planes of symmetry ($x_{mj} = a_{mj}$, $j = 1,2,3$) for 3D problems, in order to get an optimised topology characterised, at most, by an orthotropic behaviour. The presence of symmetry axes/planes implies a reduction in the design variables count, at the χth scale, according to the following formulæ:

$$n_{\chi\mathrm{var}} = \begin{cases} \prod_{i=1}^{N} \theta_{\chi i}, & \text{for B} - \text{spline entity}, \\ 2\prod_{i=1}^{N} \theta_{\chi i}, & \text{for NURBS entity}, \end{cases} \tag{33}$$

with $N = 2$ and $N = 3$ for 2D and 3D problems, respectively, and

$$\theta_{\chi i} = \begin{cases} \dfrac{n_{\chi i}+1}{2}, & \text{if } n_{\chi i} \text{ is odd}, \\ \left\lfloor \dfrac{n_{\chi i}+1}{2} \right\rfloor + 1, & \text{otherwise}, \end{cases} \tag{34}$$

where $\lfloor \cdots \rfloor$ is the floor operator.

The main goal of the numerical tests is to investigate the influence of the problem formulation, i.e., DC1, DC2 and DC3, on the flexural

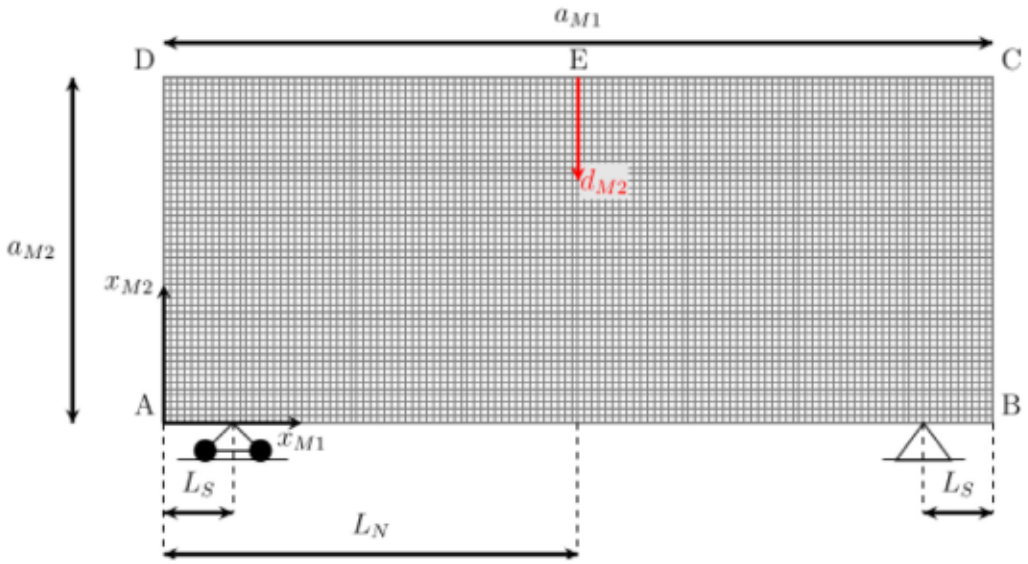

Fig. 10. Finite element model of the design domain at the macroscopic scale with its characteristic size for 2D problems.

stiffness of the optimised solution. For all benchmarks, the Rigid 4000 resin, whose physical properties are described in Section 3, is used as bulk material. Of course, all optimisation analyses are conducted under the hypothesis of small displacements and strains and by assuming a linear elastic behaviour of the Rigid 4000 resin by using the flexural modulus E_B calculated in Section 3.2, a Poisson's coefficient $\nu = 0.3$ and a density $\rho = 0.0014$ kg m^{-3}. The reference macroscopic mass of the structure and the reference macroscopic compliance are those characterising the starting solution. Moreover, the reference volume (at the generic scale) is the volume of the overall design domain of dimension D.

6.1. 2D results

Three different analyses are performed in 2D, corresponding to design cases DC1, DC2 and DC3 introduced in Section 2. In cases DC2 and DC3, the design domain of the RVE, illustrated in Fig. 9, is a square of size $L_m = 2a_{m1} = 2a_{m2} = 4$ mm. Three static analyses are performed on the FE model of the RVE to determine the elasticity tensor of the ACM at the macroscopic scale through the SEHM discussed in Section 4.2. For each analysis, the periodic BCs of Eq. (11) are applied through constraint equations among homologous nodes belonging to the opposite faces of the RVE, by considering elementary unit strains. The FE model of the RVE has been coded in the Ansys automatic parametric design language and the mesh is made of $N_{me} = 3600$ PLANE182 elements (four nodes, two DOFs per node, plane stress hypothesis with unit thickness).

For all the analyses the design domain at the macroscopic scale, shown in Fig. 10, is of rectangular shape and subject to 3PBT-like BCs. Its geometric parameters are: $a_{M1} = 100$ mm, $a_{M2} = 60$ mm, $L_S = 10$ mm and $L_N = \frac{a_{M1}}{2}$. A static analysis is conducted on the macroscopic FE model whose mesh is made of $N_{Me} = 1500$ PLANE182 elements (four nodes, two DOFs per node, plane stress hypothesis with thickness equal to 30 mm). The displacement component along x_{M2} axis is zero for the node located at $x_{M1} = L_S$, while the node located at $x_{M1} = a_{M1} - L_S$ is clamped. A vertical displacement $d_{M2} = -2$ mm is applied at $(x_{M1}, x_{M2}) = (L_N, a_{M2})$.

As stated above, when the design case DC1 is considered, only the constraint g_1 is integrated in the CNLPP of Eq. (32) and the mass fraction is set to $\gamma_{Mm} = 0.4$. The problem is solved by considering a NURBS surface characterised by $n_{MCP} = 50 \times 30$ CPs and blending functions degree $p_{Mi} = 3$, $(i = 1, 2)$. As explained in [49], this choice corresponds to a minimum length scale $d_{M\min} = 5$ mm. For DC1 the initial guess at the macroscopic scale is characterised by a uniform density field whose value is determined in order to satisfy the constraint on the macroscopic mass fraction of Eq. (29).

Regarding the design case DC2, only the constraint g_1 is integrated in the CNLPP of Eq. (32) and the mass fraction is set to $\gamma_{Mm} = 0.4$. The problem is solved by considering a NURBS surface characterised by $n_{mCP} = 31 \times 31$ CPs and blending functions degree $p_{mi} = 3$, $(i = 1, 2)$, which corresponds to a minimum length scale $d_{m\min} = 0.4$ mm at the lower scale. For DC2 the initial guess at the RVE scale is characterised by a central hole, which is generated by setting to zero the value of some CPs of the NURBS entity. Particularly, the number of CPs whose pseudo-density is zero is the result of an iterative process that stops when the constraint on the mass fraction at the macroscopic scale of Eq. (29) is met.

Finally, for DC3, problem (32) is solved by considering both constraints g_1 and g_2 and by using a mass fraction of $\gamma_{Mm} = 0.4$ at the upper scale and a volume fraction of $\gamma_{mV} = 0.3$ at the lower one. The NURBS surface is characterised by $n_{mCP} = 31 \times 31$ CPs at the RVE scale and by $n_{MCP} = 30 \times 10$ CPs at the macroscopic one, with the same value of blending function degree $p_{mi} = p_{Mi} = 3$, $(i = 1, 2)$. This choice corresponds to a minimum length scale of $d_{m\min} = 0.4$ mm at the lower scale and of $d_{M\min} = 20$ mm at the upper scale (in this way the number of RVEs included in the thinnest topological branch at the macroscopic scale is equal to $N_{\mathrm{RVE}} = 5$). For DC3 the initial guess at the RVE scale is characterised by a central hole, which is generated by setting to zero the value of some CPs of the NURBS entity. Particularly, the number of CPs whose pseudo-density is set equal to zero is the result of an iterative process that stops when the constraint on the RVE volume fraction of Eq. (30) is met. Conversely, the initial guess at the macroscopic scale is characterised by a uniform density field whose value is determined in order to satisfy the constraint on the macroscopic mass fraction of Eq. (29).

The optimised solutions are reported in Fig. 11: results are provided in terms of the number of iterations to achieve convergence (N_{iter}), of the value of reference and optimised compliance and mass, as well as of the minimum member size measured at the end of the optimisation process, i.e., $\hat{d}_{\chi,\min}$ with $(\chi = m, M)$. The macroscopic elasticity matrices related to the optimised solutions of design cases DC1, DC2 and DC3 are reported in Table 5.

From the analysis of the results, the following remarks can be inferred:

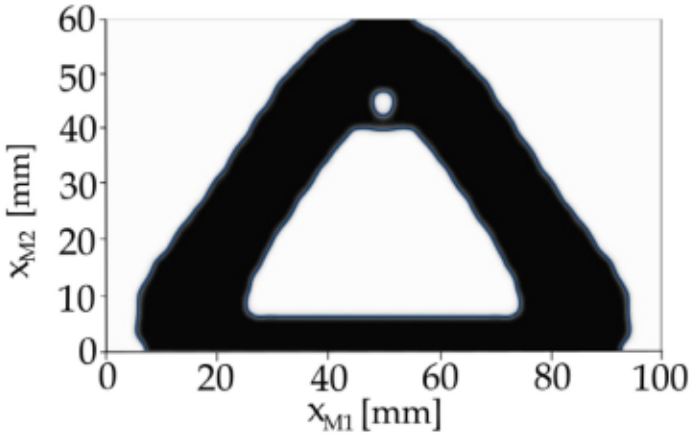

(a) $N_{\text{iter}} = 45$, $m_{M\text{opt}} = 3.32$ kg, $\mathcal{C}_{M\text{ref}} = -1983.73$Nmm, $\mathcal{C}_{M\text{opt}} = -22092.65$ Nmm, $\hat{d}_{M\text{min}} = 5$ mm

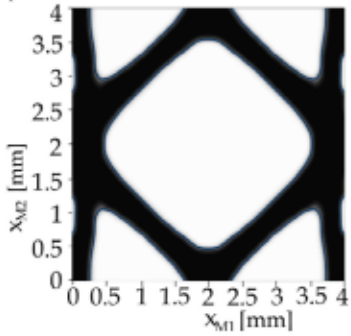

(b) $N_{\text{iter}} = 107$, $m_{M\text{opt}} = 3.32$ kg, $\mathcal{C}_{M\text{ref}} = -901.83$Nmm, $\mathcal{C}_{M\text{opt}} = -4582.27$ Nmm, $\hat{d}_{m\text{min}} = 0.4$ mm

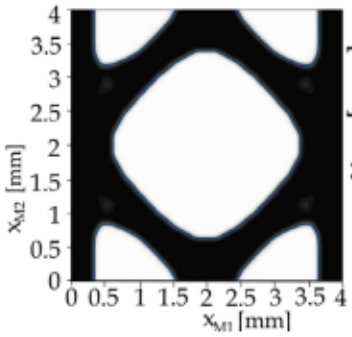

(c) $\hat{d}_{m\text{min}} = 0.4$ mm

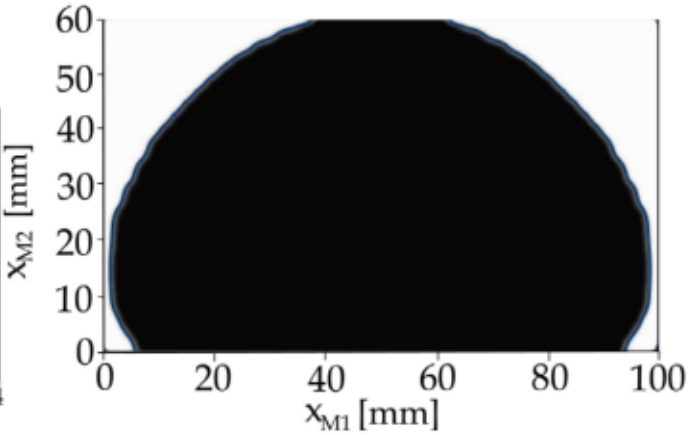

(d) $N_{\text{iter}} = 101$, $m_{M\text{opt}} = 3.32$ kg, $\mathcal{C}_{M\text{ref}} = -1529.53$Nmm, $\mathcal{C}_{M\text{opt}} = -5929.39$ Nmm, $\hat{d}_{M\text{min}} = 60$ mm

Fig. 11. 2D test case: influence of the problem formulation on the optimised topology: (a) optimised solution of DC1 (upper scale), (b) optimised solution of DC2 (lower scale), (c) optimised solution of DC3 (lower scale), (d) optimised solution of DC3 (upper scale).

1. The optimised topology obtained when considering DC1 is characterised by the highest flexural stiffness, followed by the optimised solutions of DC3 and of DC2, respectively. Particularly, this result is due to the influence of the topology at the macroscopic scale on the generalised macroscopic compliance, which is stronger than the influence of the topology at the lower scale (or, equivalently, of the influence of the equivalent homogeneous material at the macroscopic scale) on the same quantity.
2. When considering DC2 and DC3, the optimised topology at the RVE scale shows a macroscopic orthotropic behaviour with the main orthotropy axis aligned with axis x_{2M}. This is an expected result because the displacement imposed at the macroscopic scale to simulate the BCs of the 3PBT is applied along the x_{2M} axis. Moreover, the volume fraction of the optimised topology of the RVE for DC2 is lower than the volume fraction of the optimised topology of the RVE for DC3 because, the constraint on the macroscopic mass fraction being the same among the two design cases, the RVE topology of DC2 evolves towards a configuration characterised by a lower volume fraction of the

Table 5
Elasticity matrix of the optimised topologies illustrated in Fig. 11.

Design case	Stiffness matrix [MPa]
DC1	$\mathbf{C}_M = \begin{bmatrix} 5519.23 & 2365.38 & 0 \\ 2365.38 & 5519.23 & 0 \\ 0 & 0 & 1576.92 \end{bmatrix}$
DC2	$\mathbf{C}_M = \begin{bmatrix} 388.25 & 269.78 & 0 \\ 269.78 & 867.12 & 0 \\ 0 & 0 & 247.91 \end{bmatrix}$
DC3	$\mathbf{C}_M = \begin{bmatrix} 672.11 & 372.30 & 0 \\ 372.30 & 1196.43 & 0 \\ 0 & 0 & 344.07 \end{bmatrix}$

solid phase to satisfy the design requirement on the overall mass of the structure.

3. One can notice that, depending on the macroscopic loading conditions, it is not necessarily useful to formulate the TO problem by defining the topology descriptor at multiple scales. Specifically, for 3PBT-like BCs, an isotropic RVE (i.e., an RVE completely filled by the isotropic constitutive material) reveals to be the optimal solution in terms of the behaviour of the equivalent homogeneous material used at the macroscopic scale. As expected, the same topology illustrated in Fig. 11 (a) can be obtained in design case DC3, by suppressing the constraint on the volume fraction at the lower scale and by choosing the same number of CPs used in DC1 for the NURBS entity defined at the macroscopic scale. In this case, the pseudo-density at the lower scale converges towards the unit value for all the CPs of the NURBS entity, whilst the pseudo-density field at the upper scale converges exactly towards the same configuration as DC1.
4. As discussed in [49], thanks to the local support property of the NURBS basis functions, the constraint on the minimum length scale (at both lower and upper scales) is easily satisfied for all design cases without introducing an explicit optimisation constraint in the problem formulation.

6.2. 3D results

Analogously to the 2D case, three analyses are performed in the 3D case, corresponding to design cases DC1, DC2 and DC3. For DC2 and DC3, the design domain of the RVE, shown in Fig. 12, is a cube of size $L_m = 2a_{m1} = 2a_{m2} = 2a_{m3} = 4$ mm. The elasticity tensor at the macroscopic scale is assessed via six static analyses performed on the FE model of the RVE. The periodic BCs of Eq. (11) are applied through constraint equations among homologous nodes belonging to the opposite faces of the RVE, by considering elementary unit strains, for each analysis. The FE model of the RVE has been coded in the Ansys automatic parametric design language and the mesh is made of $N_{me} = 8000$ SOLID185 elements (8 nodes, 3 DOFs per node).

For all the analyses the macroscopic scale domain, shown in Fig. 13, is a parallelepiped submitted to 3PBT-like BCs. The geometrical parameters of the design domain at the macroscopic scale are: $a_{M1} = 100$ mm, $a_{M2} = 60$ mm, $a_{M3} = 30$ mm, $L_S = 10$ mm and $L_N = \frac{a_{M1}}{2}$. A static analysis is conducted on the macroscopic FE model whose mesh is made of $N_{Me} = 22\,500$ SOLID185 elements (8 nodes with 3 DOFs per node). The BCs are set as follows: $u_{M2} = u_{M3} = 0$ is set on the nodes located at $x_{M1} = L_S$, while $u_{M1} = u_{M2} = u_{M3} = 0$ is set on the nodes located at $x_{M1} = a_{M1} - L_S$. A vertical displacement $d_{M2} = -2$ mm is applied on nodes located at $(x_{M1}, x_{M2}) = (L_N, a_{M2})$.

Regarding DC1, only the constraint g_1 is integrated in the CNLPP of Eq. (32) and the mass fraction is set to $\gamma_{Mm} = 0.4$. The problem is solved by considering a NURBS hyper-surface characterised by $n_{MCP} = 25 \times 15 \times 7$ CPs and blending functions degree $p_{Mi} = 3$, $(i = 1, 2, 3)$. This choice corresponds to a minimum length scale $d_{M\min} = 5$ mm.

As far as DC2 is concerned, only the constraint g_1 is integrated in the CNLPP of Eq. (32) and the mass fraction is set to $\gamma_{Mm} = 0.4$. The problem is solved by considering a NURBS hyper-surface characterised by $n_{mCP} = 11 \times 11 \times 11$ CPs and blending functions degree $p_{mi} = 3$, $(i = 1, 2, 3)$, which corresponds to a minimum length scale $d_{m\min} = 0.4$ mm within the domain.

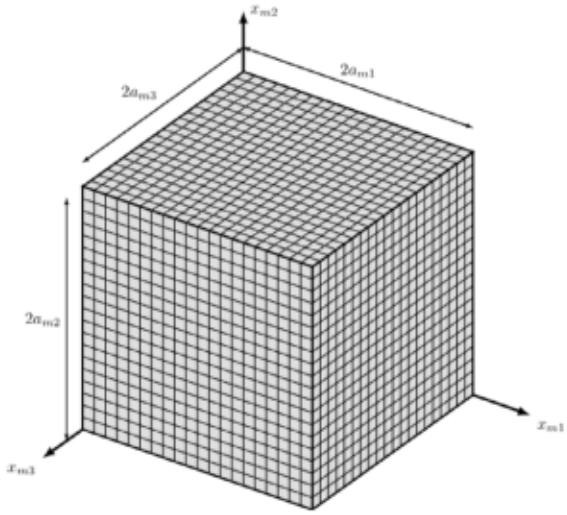

Fig. 12. Finite element model of the representative volume element with its characteristic size for 3D problems.

Finally, regarding DC3, problem (32) is solved by considering both constraints g_1 and g_2 and by using a mass fraction of $\gamma_{Mm} = 0.4$ at the upper scale and a volume fraction of $\gamma_{mV} = 0.3$ at the lower one. The NURBS hyper-surface is characterised by $n_{mCP} = 11 \times 11 \times 11$ CPs at the RVE scale and by $n_{MCP} = 15 \times 10 \times 5$ CPs at the macroscopic one, with the same value of blending function degree $p_{mi} = p_{Mi} = 3$, $(i = 1, 2, 3)$. This choice corresponds to a minimum length scale of $d_{m\min} = 0.4$ mm at the lower scale and of $d_{M\min} = 20$ mm at the upper scale.

For each design case, the initial guess at both scales is chosen by following the same procedure used in 2D analyses.

The optimised solutions are reported in Fig. 14, results are provided in terms of the number of iterations to achieve convergence (N_{iter}), of the value of reference and optimised compliance and mass as well as of the minimum member size measured at the end of the optimisation process, i.e., $\hat{d}_{\chi,\min}$ with $(\chi = m, M)$.

The macroscopic elasticity matrix related to the optimised solutions of design cases DC1, DC2 and DC3 are reported in Table 6. The same remarks done in the case of 2D analyses hold for the optimised solutions found in the 3D case.

Remark 6.1. The elasticity matrices reported in Table 6 are expressed through Voigt's notation [51]. In this study, the passage from tensor notation to Voigt's one is expressed by adopting the ANSYS convention in terms of two-way relationship among indices:

$$\{11, 22, 33, 21, 32, 31\} \Leftrightarrow \{1, 2, 3, 4, 5, 6\}. \tag{35}$$

7. Validation of the optimised topologies through three-point bending tests

In this section, the optimised topologies found in Section 6 are validated, a posteriori, through a comparison with the results of experimental tests. For the sake of brevity, only 2D optimised solutions of design cases DC1, DC2 and DC3 are printed by means of SLA technology by extruding the related geometries. Then, the 3PBT is conducted on the optimised topologies via the Zwick-Roell machine with a load capacity of 250 kN at a speed of 0.9 mm/min.

Since the optimised topology is represented by a 2D contour, a preliminary phase of reconstruction is necessary to manufacture the

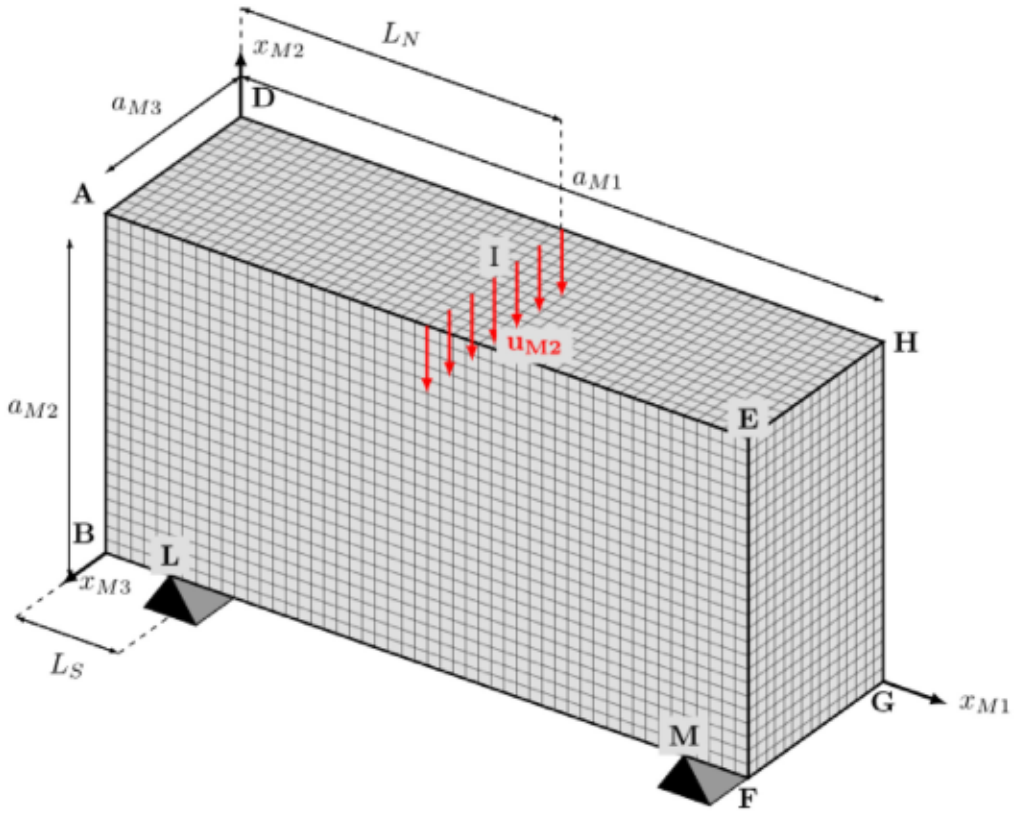

Fig. 13. Finite element model of the design domain at the macroscopic scale with its characteristic size for 3D problems.

Table 6
Elasticity matrix of the optimised topologies illustrated in Fig. 14.

Design case	Stiffness matrix
DC1	$\mathbf{C}_M = \begin{bmatrix} 5519.23 & 2365.38 & 2365.38 & 0 & 0 & 0 \\ 2365.38 & 5519.23 & 2365.38 & 0 & 0 & 0 \\ 2365.38 & 2365.38 & 5519.23 & 0 & 0 & 0 \\ 0 & 0 & 0 & 1576.92 & 0 & 0 \\ 0 & 0 & 0 & 0 & 1576.92 & 0 \\ 0 & 0 & 0 & 0 & 0 & 1576.92 \end{bmatrix}$
DC2	$\mathbf{C}_M = \begin{bmatrix} 1516.15 & 454.85 & 0.044 & 0 & 0 & 0 \\ 454.85 & 1535.71 & 0.048 & 0 & 0 & 0 \\ 0.044 & 0.044 & 0.218 & 0 & 0 & 0 \\ 0 & 0 & 0 & 532.32 & 0 & 0 \\ 0 & 0 & 0 & 0 & 0.005 & 0 \\ 0 & 0 & 0 & 0 & 0 & 0.005 \end{bmatrix}$
DC3	$\mathbf{C}_M = \begin{bmatrix} 1972.03 & 591.61 & 0.041 & 0 & 0 & 0 \\ 591.61 & 1972.22 & 0.044 & 0 & 0 & 0 \\ 0.041 & 0.044 & 0.164 & 0 & 0 & 0 \\ 0 & 0 & 0 & 690.24 & 0 & 0 \\ 0 & 0 & 0 & 0 & 0.017 & 0 \\ 0 & 0 & 0 & 0 & 0 & 0.004 \end{bmatrix}$

specimens. As discussed in [42,43], due to the use of NURBS entities to represent the topology at the lower/upper scale, the reconstruction of the boundary of the optimised topology becomes a trivial task, regardless of the DC at hand. The reconstruction phase is performed via the Catia V5 software and is shown in Fig. 15, for each design case. Of course, when the topological descriptor is defined at both lower and upper scales (DC3), the boundary of the optimised topology is obtained by combining two operations. Firstly, the RVE topology is copied along x and y axes within the macroscopic domain (rectangular pattern). Secondly, a boolean operation is performed on the rectangular pattern, i.e., the final topology is obtained by cutting the macroscopic domain filled with the RVE topologies through the contour of the optimised topology at the macroscopic scale.

Table 7
Printing parameters of the samples for each design case.

Design case	t_p [min]	n_l	V_M [mm^3]	m_{Mn} [g]	m_M [g]
DC1	255	300	76 640	106.17	102
DC2	255	300	84 410	116.94	119
DC3	420	300	81 630	113.08	114

Finally, the 3D volumes are tessellated to obtain STL files and printed via the SLA printer Form 3B® with Rigid 4000 resin as a constitutive material. The manufacturing parameters chosen to print the samples are the default ones (i.e., thickness of the layer $t_l = 0.1$ mm, thickness of the support $t_s = 2$ mm, melting thickness of the first layers $t_m = 0.3$ mm) and they are the same for all the samples. The main printing parameters related to the sample of each design case, i.e., printing time t_p, number of layers n_l, volume V_M, nominal mass m_{Mn}, actual mass m_M, are reported in Table 7, whilst the orientation and position of the samples during printing are illustrated in Fig. 16. It is noteworthy that, due to the high precision of the SLA process, the difference between nominal and real dimensions of the samples is negligible, i.e., of the order of hundredth of a millimetre.

The experimental set-up of the 3PBT for each optimised sample is shown in Fig. 17. The machine is equipped with a dedicated support to perform the 3PBT on unconventional specimens: the loading support is placed in the middle of the top face of the sample, while two supports are placed at a distance of 80 mm on the bottom surface of the sample, providing an overhang of 10 mm.

The experimental results are shown in Fig. 18 in terms of force vs. displacement curve, for each design case. One can notice that, as far as the linear part of the curves is concerned, experimental results corroborate the numerical ones discussed in Section 6, where the TO calculations are conducted assuming a linear elastic behaviour of the Rigid 4000 resin and small displacements and strains. Particularly, as it can be inferred from Fig. 18, the flexural stiffness of the optimised

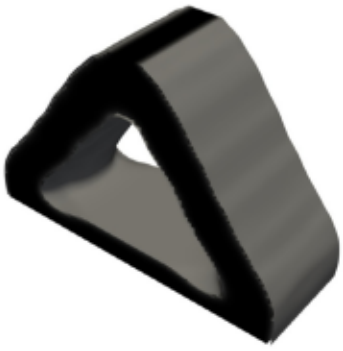

(a) $N_{\text{iter}} = 62$, $m_{M\text{opt}} = 99.7$ kg, $\mathcal{C}_{M\text{ref}} = -1963.59$ Nmm, $\mathcal{C}_{M\text{opt}} = -19922.61$ Nmm, $\hat{d}_{M\text{min}} = 5$ mm

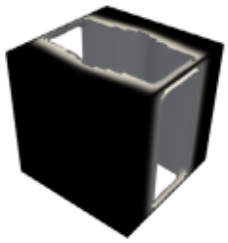

(b) $N_{\text{iter}} = 107$, $m_{M\text{opt}} = 99.7$ kg, $\mathcal{C}_{M\text{ref}} = -799.39$ Nmm, $\mathcal{C}_{M\text{opt}} = -9941.27$ Nmm, $\hat{d}_{m\text{min}} = 0.4$ mm

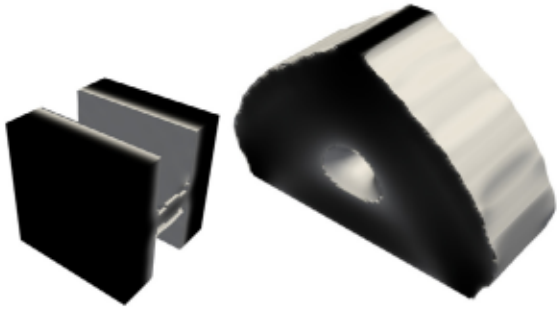

(c) $\hat{d}_{m\text{min}} = 0.4$ mm

(d) $N_{\text{iter}} = 89$, $m_{M\text{opt}} = 99.7$ kg, $\mathcal{C}_{M\text{ref}} = -4374.75$ Nmm, $\mathcal{C}_{M\text{opt}} = -12503.49$ Nmm, $\hat{d}_{M\text{min}} = 20$ mm

Fig. 14. 3D test case: influence of the problem formulation on the optimised topology: (a) optimised solution of DC1 (upper scale), (b) optimised solution of DC2 (lower scale), (c) optimised solution of DC3 (lower scale), (d) optimised solution of DC3 (upper scale).

topology solution of DC1 is the highest one, whilst the flexural stiffness of the optimised topology solution of DC3 is higher than the one of the counterpart solution of DC2.

To carry out a more correct comparison between numerical and experimental results, the optimised topologies, obtained after CAD reconstruction of the boundary, together with the supports of the 3PBT have been modelled in Ansys Workbench®. Specifically, two non-linear analyses are carried out for each design case. In the first case (indicated as NLA1), the behaviour of the resin is modelled by considering the $\sigma-\varepsilon$ curve resulting from the 3PBT conducted on the parallelepiped samples discussed in Section 3.2. In the second case (indicated as NLA2), the constitutive behaviour of the resin is modelled by exploiting the $\sigma-\varepsilon$ curve of the traction tests discussed in Section 3.1. For both cases, the non-linear behaviour of the resin is modelled through an elastoplastic multi-linear isotropic hardening law. In all the analyses, the supports are modelled by using a steel with a linear elastic isotropic behaviour having a Young's modulus $E_{\text{steel}} = 200$ GPa and a Poisson's coefficient $\nu_{\text{steel}} = 0.3$.

The FE model of the optimised topology (for each design case) used for non-linear analysis is shown in Fig. 19. In each case, PLANE182 elements (plane stress hypothesis) with a thickness equal to 30 mm are used. Due to the symmetry of each topology, only half of the geometry is modelled. The number of elements composing the FE model is $N_e = 5200$, $N_e = 170\,608$ and $N_e = 154\,933$, for DC1, DC2 and DC3, respectively. The contact regions between the supports and the sample are modelled through CONTA171 and TARGE169 elements (2D contact elements with two nodes and two DOFs per node) for the nodes belonging to the contact region of the sample and of the support, respectively. A no separation behaviour (with no friction) is assigned to the contact region and the Lagrange method is used to penalise, possibly, the initial penetration. The pinball radius of the contact region is set to 0.2 mm by following the guidelines provided in [52].

By referring to Fig. 19, the BCs are set as follows: (a) symmetry condition, i.e., $u_1 = 0$, is imposed on the nodes located on the symmetry plane; (b) $u_1 = u_2 = 0$ on the nodes belonging to the segment CD; (c) $u_2 = \delta = -0.5$ mm on the nodes belonging to the segment AB. The minimum and maximum number of sub-steps for the non-linear static analysis are set to 200 and 1000, respectively. The force vs. displacement curve obtained from analyses NLA1 and NLA2 are reported in Fig. 20 where they are compared to the experimental counterpart, for each design case. As expected, for small displacements, the force vs. displacement curve obtained when the resin is modelled by using the flexural behaviour of Fig. 6 is closer to the experimental results obtained for each optimised sample. The discrepancies between the numerical curves obtained using the flexural Young's modulus (NLA1) and the experimental ones for higher values of the displacement are related to the nature of the FE model of the specimen (2D plane stress hypothesis), which is not representative (in terms of stiffness) of the real 3D specimen used during the test. Moreover, these discrepancies are related to the constitutive law used for the resin: to correctly capture the local stress field within the structure, the constitutive law considering the difference between tension and compression should be implemented by means of a suitable user-defined material subroutine.

8. Conclusions

In this work, the optimised solutions determined through the NURBS-density-based method have been validated experimentally. Particularly, three DCs are considered: in the first case, the topological descriptor is defined solely at the upper (macroscopic) scale; in the second case, the topological variable is introduced at the lower (RVE) scale; in the last case, the topological descriptor is introduced at both scales. For each DC, the goal is to maximise the flexural stiffness subject to requirements on the lightness, on the minimum member size (related to technological constraints), and, when the topological descriptor is defined simultaneously at lower and upper scales, two further requirements are considered: the scale separation condition (to ensure the validity of the results of the SEHM) and a constraint on the volume fraction of the solid phase composing the RVE.

In each design case, the boundary conditions imposed at the macroscopic scale are those characterising the well-known 3PBT: in this way, the optimised topologies obtained at the end of the process can be easily manufactured and validated experimentally. In second and third design cases, i.e., when the topological variable is defined at the RVE scale, the scale transition is ensured via the SEHM (only weak coupling among scales is considered). Indeed, the structural responses at the upper scale depend both on the topological descriptor defined at this scale and on the one introduced at the lower scale through

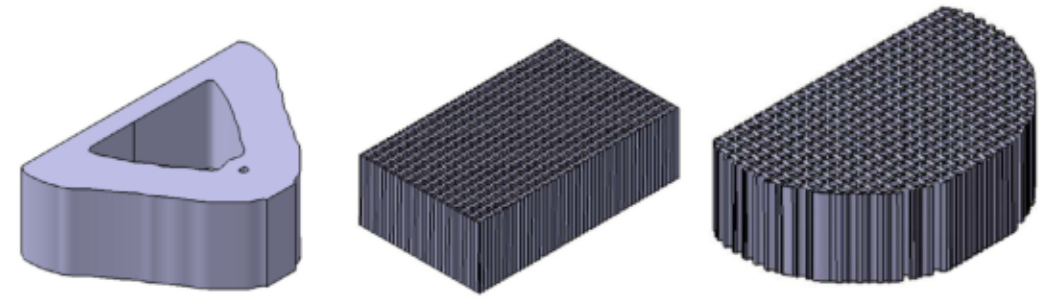

(a) DC1 (b) DC2 (c) DC3

Fig. 15. CAD model of the optimised topology for each design case.

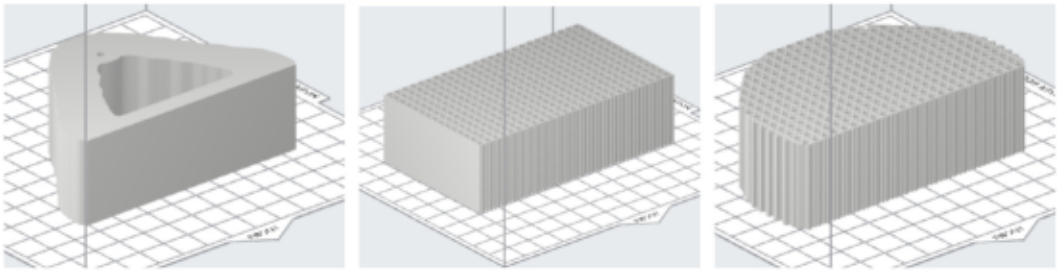

(a) DC1 (b) DC2 (c) DC3

Fig. 16. Orientation and position of the sample during printing for each design case.

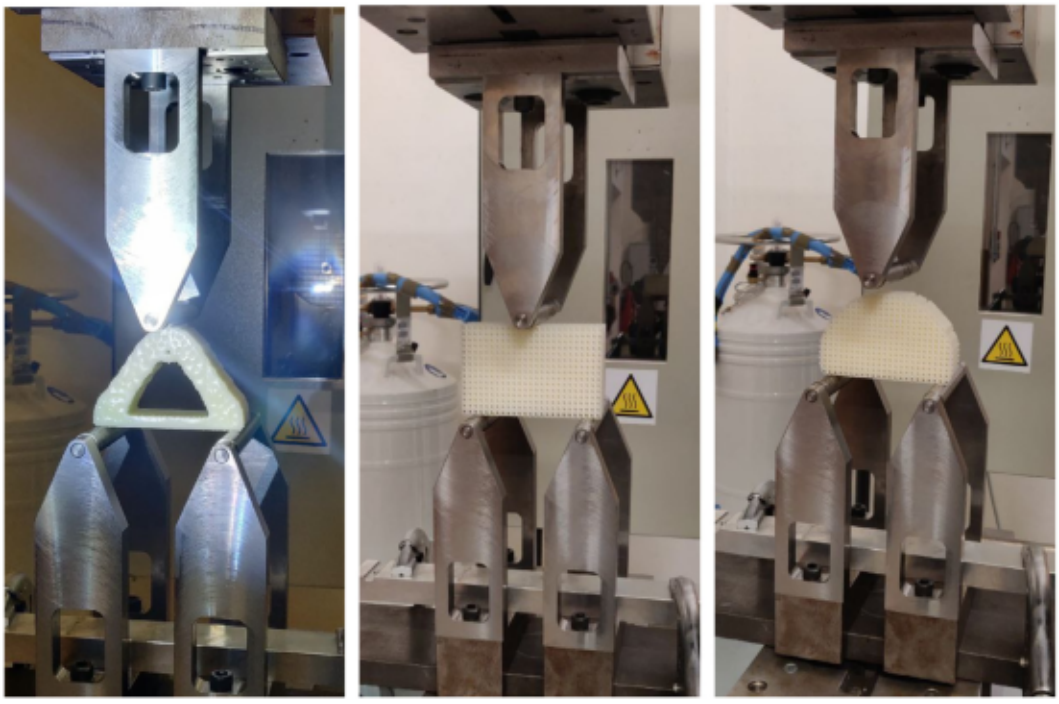

(a) DC1 (b) DC2 (c) DC3

Fig. 17. Experimental set-up of the three-point bending test for the optimised 2D topologies for each design case.

the calculation of the equivalent elasticity matrix of the fictitious homogeneous material, which replaces the RVE at the upper scale. The optimised topologies resulting from the three DCs have been printed via SLA and validated through 3PBT. Of course, a preliminary experimental campaign of tests has been conducted to characterise the behaviour (in traction and flexural) of the rigid resin constituting the constitutive material of the optimised specimens. It is noteworthy that, although the topology optimisation has been conducted by assuming a linear elastic behaviour of the material composing the specimen and under the hypothesis of small displacements and strains, the comparison between numerical and experimental results is carried out a posteriori through non-linear FE analyses on the reconstructed optimised topologies (i.e., after reconstruction of their boundary).

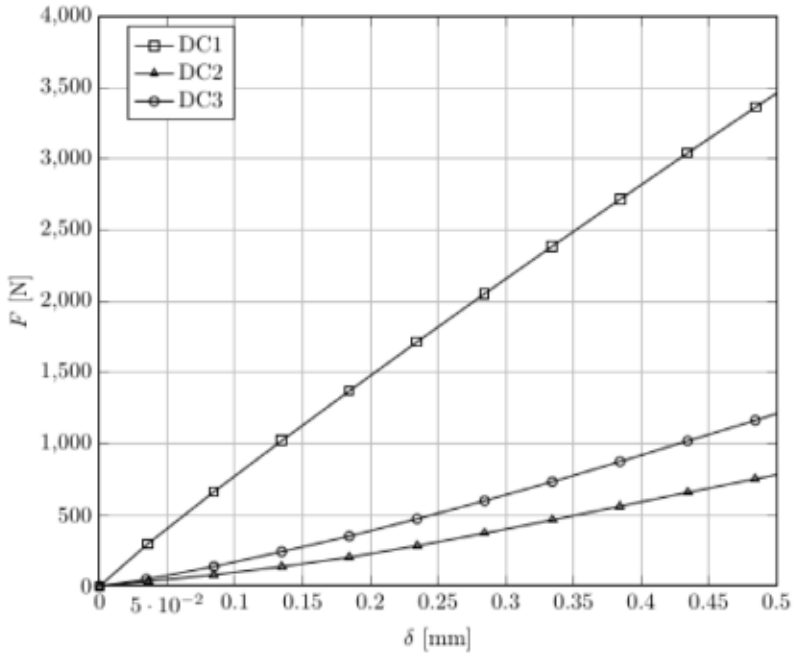

Fig. 18. Force vs. displacement curve obtained from three-point bending test on the optimised sample of each design case.

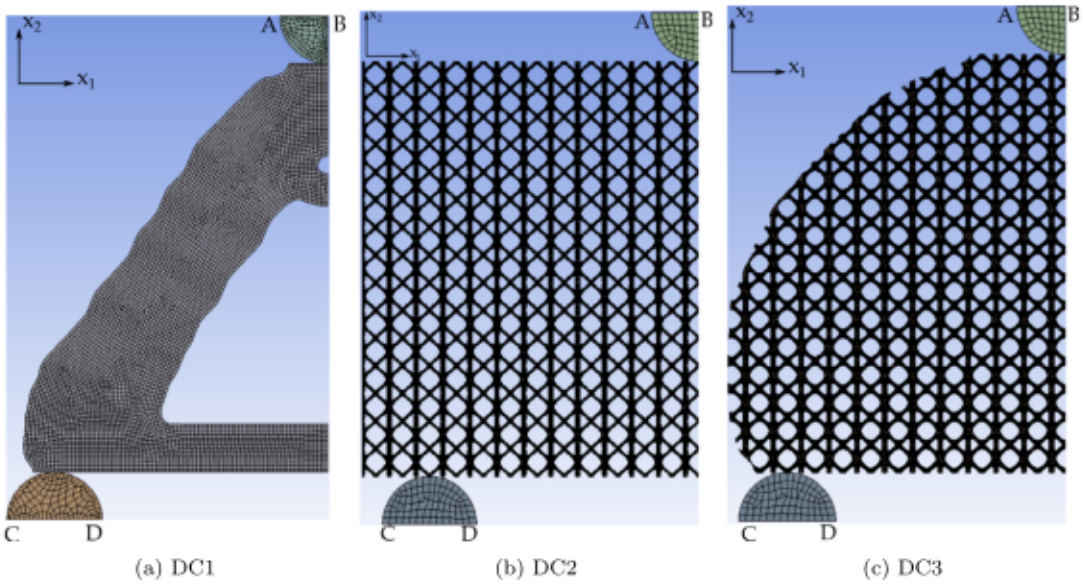

Fig. 19. Finite element model and boundary conditions for the non-linear analysis conducted a posteriori on the optimised samples (for each design case).

Some features of the proposed methodology need to be highlighted after a careful analysis of the numerical results.

Firstly, some advantages of the NURBS formalism can be clearly identified: (a) since the topological descriptor introduced at each scale is a NURBS entity, the final solution does not depend upon the quality of the mesh of the finite element model; (b) unlike classical density-based approaches, there is no need to define a further filter zone, since the NURBS local support property establishes an implicit relationship among contiguous elements of the mesh; (c) when compared to classical density-based approaches, the number of design variables is reduced; (d) since the pseudo-density field at the generic scale is described through NURBS entities, the boundary of the topology is available at each iteration of the optimisation process, thus, the integration of constraints of geometric nature (e.g., on the local curvature of the boundary, on the local direction of the tangent vector, maximum member size, etc.) in the problem formulation and the CAD reconstruction phase of the boundary of the optimised topology become easy tasks; (e) of course, the optimised topology depends upon the NURBS integer parameters, i.e., number of control points and degrees of Bernstein's polynomials, which have a direct impact on the size of the local support of the blending functions.

Secondly, the best performances, in terms of flexural stiffness, are obtained in the first design case wherein the topological descriptor is introduced only at the macroscopic scale. This means that, as far as the 3PBT is concerned, the optimised topology is characterised by an isotropic material filling the whole RVE and optimally distributed at the macroscopic scale. This is confirmed also by the results of second and third design cases, which highlight that, to satisfy the requirements of the problem at hand and to withstand the applied loads, both the RVE topology and the macroscopic one evolve towards a configuration optimising the macroscopic elastic response of the continuum, as well

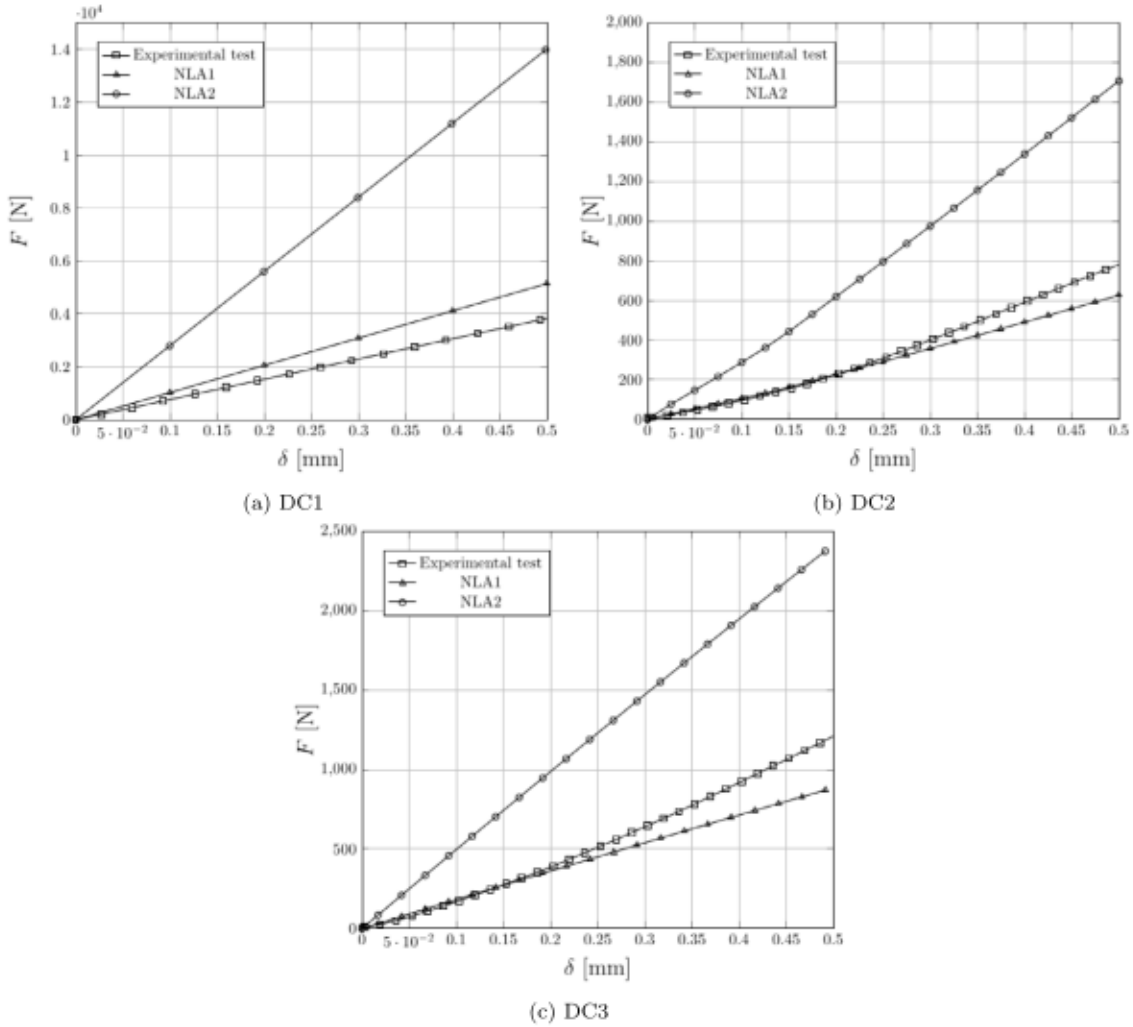

Fig. 20. Force vs. displacement curves for each design case by considering different material behaviours for the Rigid 4000 resin.

as the material distribution at the upper scale. However, since the lightness requirement and the constraint on the volume fraction of the solid phase are introduced, the optimised topology at the RVE scale cannot converge towards the isotropic solution. Of course, when considering the most general problem formulation, i.e., the one involving the topological descriptor at both scales, when the constraint on the volume fraction of the solid phase at the RVE scale is suppressed and only the one on the overall mass of the structure is kept, the optimised solution coincide with the one of the first design case (wherein the topological descriptor is defined solely at the upper scale).

Thirdly, the effect of the minimum length scale requirement on the optimised solution at each problem scale is correctly taken into account, without the need of introducing an explicit optimisation constraint. Indeed, this requirement can be easily fulfilled by properly setting the integer parameters of the NURBS entity representing the topological variable at each scale.

Finally, regarding the comparison between numerical and experimental results obtained on the optimised topologies (for each design case), in terms of force vs. displacement curve, the utilisation of the non-linear constitutive law of the rigid resin as well as the modelling of the contact regions between the sample and the supports of the testing machine allows obtaining a good agreement between numerical and experimental curves only when the $\sigma - \varepsilon$ curve describing flexural behaviour of the resin is used. Nevertheless, some discrepancies between numerical and experimental results can be observed for some values of the applied displacement. To obtain better (and more consistent) results, the complete compression–traction curve describing the true behaviour of the rigid resin should be modelled via a user-defined material routine and a 3D numerical model should be considered instead of a 2D model based on plane stress hypothesis. However, this task does not fall within the scopes of the present work and could constitute a prospect of this study.

A further prospect of this work is about the integration of the non-linear behaviour of the bulk material within the TO process, by developing also a suitable non-linear homogenisation strategy (as far as second and third design cases are concerned). Finally, suitable failure criteria at upper and lower scales should be derived and integrated into the multi-scale TO problem formulation for the homogeneous anisotropic material at the macroscopic scale and for the bulk material at the RVE scale in order to optimise not only the stiffness of the structure but also its strength.

CRediT authorship contribution statement

Marco Montemurro: Conceptualisation, Methodology, Software, Validation, Writing – original draft, Writing – review & editing, Supervision, Funding acquisition. **Giulia Bertolino:** Methodology, Software, Investigation, Writing – original draft, Experiments. **Enrico Panettieri:** Experiments, Supervision.

Declaration of competing interest

The authors declare that they have no known competing financial interests or personal relationships that could have appeared to influence the work reported in this paper.

Data availability

The raw/processed data required to reproduce these findings cannot be shared at this time as the data also forms part of an ongoing study.

Acknowledgements

G. Bertolino is grateful to French National Research Agency for funding this study through the research project COFFA (Conception et Optimisation de Forme pour la Fabrication Additive) ANR-17-CE10-0008.

Appendix. Gradient of the objective function and of the optimisation constraints

When differentiating the generalised compliance C_M of Eq. (24) with respect to ξ^g_{mi} $(i = 1, 2)$ one obtains:

$$\frac{\partial C_M}{\partial \xi^g_{mik_m}} = -\sum_{e=1}^{N_{Me}} \sum_{q=1}^{6} \sum_{r=1}^{6} \frac{\partial C_{Mqr}}{\partial \xi^g_{mik_m}} \varepsilon_{Meq} \varepsilon_{Mer} V_{Me}, \; i = 1, 2, \; k_m = 1, \dots, n_{\mathrm{mCP}}, \tag{A.1}$$

with

$$\frac{\partial C_{Mqr}}{\partial \xi^g_{mik_m}} = \begin{cases} \dfrac{1}{V_{\mathrm{RVE}} \left(\varepsilon^0_{mq}\right)^2} \displaystyle\sum_{e \in S_{mk_m}} \frac{\alpha}{\rho_{me}} \frac{\partial \rho_{me}}{\partial \xi^g_{mik_m}} \mathcal{W}_{me}\left(\varepsilon^0_{mq}\right), \; \text{if } q = r, \\ \dfrac{1}{2V_{\mathrm{RVE}} \varepsilon^0_{mq} \varepsilon^0_{mr}} \displaystyle\sum_{e \in S_{mk_m}} \frac{\alpha}{\rho_{me}} \frac{\partial \rho_{me}}{\partial \xi^g_{mik_m}} \mathcal{W}_{me}\left(\varepsilon^0_{mq}, \varepsilon^0_{mr}\right) - \\ \qquad \dfrac{\varepsilon^0_{mq}}{2\varepsilon^0_{mr}} \dfrac{\partial C_{Mqq}}{\partial \xi^g_{mik_m}} - \dfrac{\varepsilon^0_{mr}}{2\varepsilon^0_{mq}} \dfrac{\partial C_{Mrr}}{\partial \xi^g_{mik_m}}, \; \text{if } q \neq r. \end{cases} \tag{A.2}$$

In Eq. (A.1), ε_{Meq} $(q = 1, \dots, 6)$ is the qth component of the strain vector (Voigt's notation) of the generic element e of the FE model at the macroscopic scale, whilst V_{Me} is its volume. In Eq. (A.2), ε^0_{mq} is the qth elementary strain imposed on the RVE through the periodic BCs of Eq. (11) and $\mathcal{W}_{me}$ is the work of internal forces of the generic element of the FE model of the RVE.

The gradient of the macroscopic compliance with respect to the topological variable at the upper scale reads:

$$\frac{\partial C_M}{\partial \xi^g_{Mik_M}} = -\alpha \sum_{e \in S_{Mk_M}} \frac{\mathcal{W}_{Me}}{\rho_{Me}} \frac{\partial \rho_{Me}}{\partial \xi^g_{Mik_M}}, \; i = 1, 2, \; k_M = 1, \dots, n_{MCP}, \tag{A.3}$$

where $\mathcal{W}_{Me}$ is the internal work of the generic element of the FE model at the macroscopic scale. In Eqs. (A.1)–(A.3), the linear index k_χ $(\chi = m, M)$ has been introduced for the sake of compactness. The relation between k_χ and $i_{\chi j}$, $(j = 1, 2, 3)$ is:

$$k_\chi := 1 + i_{\chi 1} + i_{\chi 2}(n_{\chi 1} + 1) + i_{\chi 3}(n_{\chi 1} + 1)(n_{\chi 2} + 1), \; \chi = m, M. \tag{A.4}$$

Moreover, in Eqs. (A.1)–(A.3), the quantity $S_{\tau k_\tau}$ $(\tau = m, M)$ is the discretised version of the local support of Eq. (10), while $\dfrac{\partial \rho_{\tau e}}{\partial \xi^g_{\tau i k_\tau}}$ reads:

$$\frac{\partial \rho_{\tau e}}{\partial \xi^g_{\tau i k_\tau}} = \begin{cases} R_{k_\tau e}, \; \text{if } i = 1, \\ \dfrac{R_{k_\tau e}}{\xi^g_{\tau 2 k_\tau}} \left(\xi^g_{\tau 1 k_\tau} - \rho_{\tau e}\right), \; \text{if } i = 2. \end{cases} \tag{A.5}$$

The scalar quantity $R_{k_\tau e}$ appearing in Eq. (A.5) is the NURBS rational basis function of Eq. (3) evaluated at the element centroid.

Regarding the optimisation constraints, by differentiating Eqs. (27), (26) and (30) one obtains:

$$\begin{aligned} &\frac{\partial V_M}{\partial \xi^g_{mik_m}} = 0, \; i = 1, 2, \; k_m = 1, \dots, n_{\mathrm{mCP}}, \\ &\frac{\partial V_M}{\partial \xi^g_{Mik_M}} = \sum_{e \in S_{Mk_M}} V_{Me} \frac{\partial \rho_{Me}}{\partial \xi^g_{Mik_M}}, \; i = 1, 2, \; k_M = 1, \dots, n_{MCP}, \end{aligned} \tag{A.6}$$

$$\begin{aligned} &\frac{\partial m_M}{\partial \xi^g_{mik_m}} = \frac{\tau_m V_M}{V_{\mathrm{RVE}}} \sum_{e \in S_{mk_m}} V_{me} \frac{\partial \rho_{me}}{\partial \xi^g_{mik_m}}, \; i = 1, 2, \; k_m = 1, \dots, n_{\mathrm{mCP}}, \\ &\frac{\partial m_M}{\partial \xi^g_{Mik_M}} = \tau_M \frac{\partial V_M}{\partial \xi^g_{Mik_M}}, \; i = 1, 2, \; k_M = 1, \dots, n_{MCP}, \end{aligned} \tag{A.7}$$

$$\begin{aligned} &\frac{\partial V_m}{\partial \xi^g_{mik_m}} = \sum_{e \in S_{mk_m}} V_{me} \frac{\partial \rho_{me}}{\partial \xi^g_{mik_m}}, \; i = 1, 2, \; k_m = 1, \dots, n_{\mathrm{mCP}}, \\ &\frac{\partial V_m}{\partial \xi^g_{Mik_M}} = 0, \; i = 1, 2, \; k_M = 1, \dots, n_{MCP}. \end{aligned} \tag{A.8}$$

References

[1] Tang Y, Zhao YF. Multifunctional design of heterogeneous cellular structures. Struct Multidiscip Optim 2018;58(3):1121–38. http://dx.doi.org/10.1007/s00158-018-1956-9.

[2] Benedetti M, du Plessis A, Ritchie R, Dallago M, Razavi S, Berto F. Architected cellular materials: A review on their mechanical properties towards fatigue-tolerant design and fabrication. Mater Sci Eng R 2021;144:100606. http://dx.doi.org/10.1016/j.mser.2021.100606.

[3] Collet M, Noël L, Bruggi M, Duysinx P. Topology optimization for microstructural design under stress constraints. Struct Multidiscip Optim 2018;58(6):2677–95.

[4] Borovinšek M, Novak N, Vesenjak M, Ren Z, Ulbin M. Designing 2D auxetic structures using multi-objective topology optimization. Mater Sci Eng A 2020;795:139914. http://dx.doi.org/10.1016/j.msea.2020.139914.

[5] Wallin M, Tortorelli D. Nonlinear homogenization for topology optimization. Mech Mater 2020;145:103324. http://dx.doi.org/10.1016/j.mechmat.2020.103324.

[6] Montemurro M, Bertolino G, Roiné T. A general multi-scale topology optimisation method for lightweight lattice structures obtained through additive manufacturing technology. Compos Struct 2021;258:113360. http://dx.doi.org/10.1016/j.compstruct.2020.113360.

[7] Huang J, Xu S, Ma Y, Liu J. A topology optimization method for hyperelastic porous structures subject to large deformation. Int J Mech Mater Des 2021. http://dx.doi.org/10.1007/s10999-021-09576-4.

[8] Wu Z, Fan F, Xiao R, Yu L. The substructuring-based topology optimization for maximizing the first eigenvalue of hierarchical lattice structure. Internat J Numer Methods Engrg 2020;121(13):2964–78. http://dx.doi.org/10.1002/nme.6342.

[9] Hoang V-N, Nguyen N-L, Tran P, Qian M, Nguyen-Xuan H. Adaptive concurrent topology optimization of cellular composites for additive manufacturing. JOM 2020;72(6):2378–90. http://dx.doi.org/10.1007/s11837-020-04158-9.

[10] Jia J, Da D, Loh C-L, Zhao H, Yin S, Xu J. Multiscale topology optimization for non-uniform microstructures with hybrid cellular automata. Struct Multidiscip Optim 2020;62(2):757–70. http://dx.doi.org/10.1007/s00158-020-02533-3.

[11] Wang Y, Hu D, Wang H, Zhang T, Yan H. Practical design optimization of cellular structures for additive manufacturing. Eng Optim 2020;52(11):1887–902. http://dx.doi.org/10.1080/0305215X.2019.1696785.

[12] Liu P, Kang Z, Luo Y. Two-scale concurrent topology optimization of lattice structures with connectable microstructures. Addit Manuf 2020;36:101427.

[13] Wu J, Wang W, Gao X. Design and optimization of conforming lattice structures. IEEE Trans Vis Comput Graphics 2021;27(1):43–56. http://dx.doi.org/10.1109/TVCG.2019.2938946.

[14] Li Q, Xu R, Liu J, Liu S, Zhang S. Topology optimization design of multi-scale structures with alterable microstructural length-width ratios. Compos Struct 2019;230. http://dx.doi.org/10.1016/j.compstruct.2019.111454.

[15] Li L, Du Z, Kim H. Design of architected materials for thermoelastic macrostructures using level set method. JOM 2020;72(4):1734–44. http://dx.doi.org/10.1007/s11837-020-04046-2.

[16] Xia Q, Zong H, Shi T, Liu H. Optimizing cellular structures through the M-VCUT level set method with microstructure mapping and high order cutting. Compos Struct 2021;261. http://dx.doi.org/10.1016/j.compstruct.2020.113298.

[17] Kijanski W, Barthold F-J. Two-scale shape optimisation based on numerical homogenisation techniques and variational sensitivity analysis. Comput Mech 2021;67(4):1021–40. http://dx.doi.org/10.1007/s00466-020-01955-6.

[18] Bertolino G, Montemurro M. Two-scale topology optimisation of cellular materials under mixed boundary conditions. Int J Mech Sci 2022;216:106961. http://dx.doi.org/10.1016/j.ijmecsci.2021.106961.

[19] Teimouri M, Mahbod M, Asgari M. Topology-optimized hybrid solid-lattice structures for efficient mechanical performance. Structures 2021;29:549–60.
[20] Cai Q, Feng R, Zhang Z. Topology optimization of truss structure considering nodal stability and local buckling stability. Structures 2022;40:64–73.
[21] Cai Q, Feng R, Zhang Z. Topology optimization of trusses incorporating practical local buckling stability considerations. Structures 2022;41:1710–8.
[22] Sivapuram R, Dunning PD, Kim HA. Simultaneous material and structural optimization by multiscale topology optimization. Struct Multidiscip Optim 2016;54(5):1267–81. http://dx.doi.org/10.1007/s00158-016-1519-x.
[23] Gao J, Li H, Gao L, Xiao M. Topological shape optimization of 3D micro-structured materials using energy-based homogenization method. Adv Eng Softw 2018;116:89–102. http://dx.doi.org/10.1016/j.advengsoft.2017.12.002.
[24] Wang Y, Xu H, Pasini D. Multiscale isogeometric topology optimization for lattice materials. Comput Methods Appl Mech Engrg 2017;316:568–85. http://dx.doi.org/10.1016/j.cma.2016.08.015.
[25] Wang L, Zhao X, Liu D. Size-controlled cross-scale robust topology optimization based on adaptive subinterval dimension-wise method considering interval uncertainties. Eng Comput 2022. http://dx.doi.org/10.1007/s00366-022-01615-8.
[26] Wang L, Zhao X, Wu Z, Chen W. Evidence theory-based reliability optimization for cross-scale topological structures with global stress, local displacement, and micro-manufacturing constraints. Struct Multidiscip Optim 2022;65:23.
[27] Wang L, Liu Y, Liu D, Wu Z. A novel dynamic reliability-based topology optimization (DRBTO) framework for continuum structures via interval-process collocation and the first-passage theories. Comput Methods Appl Mech Engrg 2021;386:114107.
[28] Wang L, Liu Y, Li M. Time-dependent reliability-based optimization for structural-topological configuration design under convex-bounded uncertain modeling. Reliab Eng Syst Saf 2022;221:108361.
[29] Xia L, Breitkopf P. Concurrent topology optimization design of material and structure within nonlinear multiscale analysis framework. Comput Methods Appl Mech Engrg 2014;278:524–42. http://dx.doi.org/10.1016/j.cma.2014.05.022.
[30] Xu J, Gao L, Xiao M, Gao J, Li H. Isogeometric topology optimization for rational design of ultra-lightweight architected materials. Int J Mech Sci 2020;166:105103. http://dx.doi.org/10.1016/j.ijmecsci.2019.105103.
[31] Du Y, Li H, Luo Z, Tian Q. Topological design optimization of lattice structures to maximize shear stiffness. Adv Eng Softw 2017;112:211–21. http://dx.doi.org/10.1016/j.advengsoft.2017.04.011.
[32] Wu J, Sigmund O, Groen J. Topology optimization of multi-scale structures: a review. Struct Multidiscip Optim 2021;63(3):1455–80. http://dx.doi.org/10.1007/s00158-021-02881-8.
[33] Mohan SR, Simhambhatla S. Adopting feature resolution and material distribution constraints into topology optimisation of additive manufacturing components. Virtual Phys Prototyp 2018;14(1):79–91. http://dx.doi.org/10.1080/17452759.2018.1501275.
[34] Rashid R, Masood S, Ruan D, Palanisamy S, Huang X, Rashid RR. Topology optimisation of additively manufactured lattice beams for three-point bending test. In: 2018 annual international solid freeform fabrication symposium. 2018.
[35] Zhang J, Yanagimoto J. Topology optimization of microlattice dome with enhanced stiffness and energy absorption for additive manufacturing. Compos Struct 2021;255:112889. http://dx.doi.org/10.1016/j.compstruct.2020.112889.
[36] Zhang Y, Xiao M, Zhang X, Gao L. Topological design of sandwich structures with graded cellular cores by multiscale optimization. Comput Methods Appl Mech Engrg 2020;361:112749. http://dx.doi.org/10.1016/j.cma.2019.112749.
[37] Kim J-E, Park K. Multiscale topology optimization combining density-based optimization and lattice enhancement for additive manufacturing. Int J Precis Eng Manuf-Green Technol 2020;8(4):1197–208. http://dx.doi.org/10.1007/s40684-020-00289-1.
[38] Costa G, Montemurro M, Pailhès J. A 2D topology optimisation algorithm in NURBS framework with geometric constraints. Int J Mech Mater Des 2018;14(4):669–96.
[39] Costa G, Montemurro M, Pailhès J. NURBS Hypersurfaces for 3D Topology Optimisation Problems. Mech Adv Mater Struct 2021;28(7):665–84.
[40] Montemurro M. On the structural stiffness maximisation of anisotropic continua under inhomogeneous Neumann-Dirichlet boundary conditions. Compos Struct 2022;287:115289. http://dx.doi.org/10.1016/j.compstruct.2022.115289.
[41] ASTM. Standard test methods for flexural properties of unreinforced and reinforced plastics and electrical insulating materials. ASTM International; 2003, http://dx.doi.org/10.1520/D0790-03.
[42] Bertolino G, Montemurro M, Perry N, Pourroy F. An efficient hybrid optimization strategy for surface reconstruction. Comput Graph Forum 2021;40(6):215–41. http://dx.doi.org/10.1111/cgf.14269.
[43] Costa G, Montemurro M, Pailhès J. A general hybrid optimization strategy for curve fitting in the non-uniform rational basis spline framework. J Optim Theory Appl 2017;176(1):225–51.
[44] Korshunova N, Alaimo G, Hosseini S, Carraturo M, Reali A, Niiranen J, Auricchio F, Rank E, Kollmannsberger S. Bending behavior of octet-truss lattice structures: Modelling options, numerical characterization and experimental validation. Mater Des 2021;205:109693. http://dx.doi.org/10.1016/j.matdes.2021.109693.
[45] ASTM. Standard test method for compressive properties of rigid plastics. ASTM International; 2016, http://dx.doi.org/10.1520/D0695-15.
[46] ASTM. Standard test method for tensile properties of plastics. ASTM International; 2017, http://dx.doi.org/10.1520/D0638-14.
[47] Piegl L, Tiller W. The NURBS book. Berlin, Heidelberg, New York: Springer-Verlag; 1997.
[48] Barbero E. Finite element analysis of composite materials. Taylor & Francis Group: CRC Press; 2007.
[49] Costa G, Montemurro M, Pailhès J. Minimum Length Scale Control in a NURBS-based SIMP Method. Comput Methods Appl Mech Engrg 2019;354:63–989.
[50] Svanberg K. A class of globally convergent optimization methods based on conservative convex separable approximations. SIAM J Optim 2002;12(2):555–73. http://dx.doi.org/10.1137/s1052623499362822.
[51] Jones RM. Mechanics of composite materials. McGraw-Hill; 1975.
[52] ANSYS. ANSYS® academic research mechanical, release 21.1, contact technology guide. ANSYS, Inc.; 2004.